Journal of Atmospheric and Solar–Terrestrial Physics 219 (2021) 105616

Contents lists available at ScienceDirect

Journal of Atmospheric and Solar-Terrestrial Physics

journal homepage: www.elsevier.com/locate/jastp

The Dynamics of the Alfvénic Oval

Andreas Keiling

University of California, Berkeley, CA, USA

A R T I C L E I N F O

Keywords:
Alfvén wave
Magnetosphere-ionosphere coupling
Wave-particle interaction
Energy transport
Geomagnetic activity
Aurora

A B S T R A C T

The auroral oval is a well-established concept, introduced more than five decades ago. The Alfvénic oval, on the other hand, is a very recent concept, which has been revealed in both observational and numerical studies. This is the first review of the global Alfvénic oval, while also defining primary, secondary and tertiary layers of the Alfvénic oval. The focus lies on the large-scale dynamic properties of the global Alfvénic oval in relation to the *AE* index, substorm phases, storm phases and solar wind/IMF conditions. Statistical data recorded above and below the nominal auroral acceleration region are reviewed, together with results from global simulation studies. The Alfvénic oval's relation to the auroral oval is also reviewed. This review demonstrates that the Alfvénic oval is well enough defined and investigated to give it its name, and it demonstrates that our understanding allows for the prediction of the Alfvénic oval under various conditions.

1. Introduction and outline

Alfvén waves are abundant in the magnetosphere and play many roles in its dynamics. Guided along magnetic field lines, Alfvén waves carry energy from one region to another, most notably towards the auroral acceleration region (AAR), a key region for magnetosphere-ionosphere (M-I) coupling. Alfvén waves constitute an energy sink for other forms of energy in the magnetosphere, thereby helping to release overloading and stresses, a role related to the generation of Alfvén waves. Alfvén waves carry field-aligned currents (FACs) and are also necessary for the establishment of quasi-static FACs (also called Birkeland currents). Ultra-low frequency (ULF) pulsations on the ground and in space encompass a broad range of wave phenomena, some of which are associated with Alfvén waves. The transfer of energy from large magnetohydrodynamic (MHD) scales to smaller kinetic scales is important for the dissipation of Alfvén wave energy. Alfvén waves are an effective accelerator of both electrons and ions, some of which contribute to the aurora. Alfvén waves have been proposed to mediate reconnection. These are some of the applications of Alfvén waves, which extend beyond Earth's magnetosphere.

The growing recognition of the *global* role and *global* impact of Alfvén waves in the dynamics of the magnetosphere led to the concept of a global *Alfvénic Oval* (Keiling et al., 2019b). This concept evolved from independent statistical studies, which showed the global morphology of Alfvén waves from space, using different satellites at different altitudes (Ivchenko and Marklund, 2001; Chaston et al., 2003; Keiling et al., 2003). Subsequent studies (references below) detailed many of the Alfvénic oval's dynamic properties. In this review, we outline the dynamics of the Alfvénic oval as a global phenomenon. Details of Alfvén wave dynamics pertaining to wave-particle interaction, energy cascades, pulsations, field line resonance (FLR), and smaller-scale auroral structures, as studied in individual case studies and numerical/theoretical studies, can be found in other reviews (e.g., Saito, 1969; Southwood and Hughes, 1983; Glassmeier et al., 1999; Stasiewicz et al., 2000; Chaston, 2006; and Keiling, 2009).

The auroral oval has long provided a reference frame for other phenomena or features, such as Birkeland currents, auroral forms, ionospheric convection, and magnetospheric boundaries. The Alfvénic oval is similarly related to the auroral oval. Hence, we start out by briefly describing the auroral oval in section 1.1. The development of the concept of the auroral oval is reviewed in great detail by Feldstein and Galperin (1985), from the first all-sky camera films to the first images from satellite observatories.

In section 1.2, we define the term "Alfvénic oval" and provide the initial justification for its introduction and usefulness, which is then further cemented in the subsequent sections. This subsection is most important to follow the thrust and philosophy of this review, and the reader is advised not to skip it.

Alfvén waves interact with the AAR and couple through the AAR to the ionosphere. Such coupling can also be observed for the Alfvénic oval. It is clear that the AAR has profound effects on the evolution of the Alfvénic oval. While we largely treat the AAR as a "black box" in this review, some aspects of the AAR, especially as they relate to Alfvénic M-I coupling, are provided as a reference in section 1.3.

E-mail address: keiling@berkeley.edu.

https://doi.org/10.1016/j.jastp.2021.105616
Received 15 June 2020; Received in revised form 19 February 2021; Accepted 11 March 2021
Available online 18 March 2021

Section 2 is the main part of this review, where the global dynamical behavior of the Alfvénic oval is reviewed. In particular, we look at dependences on the auroral electroject (*AE*) index, phases of substorms and storms, and solar wind and interplanetary magnetic field (IMF) parameters. Simulation studies have contributed to the description and understanding of the Alfvénic oval and are also reviewed. In this section, the focus is on Alfvén wave and Alfvénically-accelerated electron statistics. Below, we define both parts, respectively, as primary and secondary Alfvénic ovals.

The (visible) auroral oval comprises different types of auroral excitation, driven by precipitating ions and electrons with different characteristics. The degree to which the auroral oval is globally comprised of the Alfvénic aurora under various geomagnetic conditions is reviewed in section 3. Below, we define this part as the tertiary Alfvénic oval, which exclusively refers to the portion of the visible aurora that is driven by Alfvénically-accelerated electron precipitation.

The ultimate goal of this review is to address the following questions: Is the Alfvénic oval a valid concept? How does the Alfvénic oval respond to changes in geomagnetic conditions? Are the morphology and energy balance of the reported Alfvénic ovals consistent at different altitudes? How much does the Alfvénic oval contribute to the overall energy flow in M-I coupling? Can the Alfvénic oval be predicted? In what areas do we need to advance to better understand the Alfvénic oval? In light of this review, we will address these questions in section 4, the final section of this review.

1.1. *Auroral oval*

The auroral oval is the luminous band that encircles both the northern and southern magnetic poles (Feldstein, 1963). It is not a uniform band, but rather, it comprises smaller-scale structures embedded within it (review by Akasofu, 2012). Furthermore, it is not always continuous or closed (Feldstein and Starkov, 1967), as the word "oval" might imply. Especially during northward IMF, the auroral oval is in parts subvisual (Akasofu, 1989), not showing its oval characteristics. The global auroral oval shrinks and expands with geomagnetic activity (Akasofu and Chapman, 1963; Feldstein and Starkov, 1967). The auroral oval shows asymmetries between the dayside and nightside, and between east and west (review by Karlsson et al., 2017). While showing great variability, it also reveals repeatable patterns that have led to an improved understanding. One of the most dramatic instances of such variability occurs during a geomagnetic storm. Fig. 1 shows 10 min during which the aurora changes from faint to intense brightness in a band around the magnetic pole. Another example of a repeatable pattern is the auroral substorm (see section 2.2).

The auroral oval has been and still is the visible "window" into the magnetosphere, where the aurora-causing dynamic events occur. Of course, auroral/magnetospheric scientists have "looked" beyond the window to explore the magnetosphere *in situ* and have established many physical connections between magnetospheric processes and individual auroral features in the ionosphere (e.g., see monographs by Keiling et al., 2012; Zhang and Paxton, 2016). Being a projection of magnetospheric processes, auroral variability tells us that the magnetosphere and its interactions are incredibly complex. Even as recently as last year, new features in the aurora have been discovered (Palmroth et al., 2020), thus forcing us to continue our quest for explanations. Although there have been enormous advances over the last five decades covering the space age, making sense of the complex aurora is something that will occupy scientists for many decades to come.

In spite of such complexity, several studies provide predictions (forecasts) of the location, size, and global power of the auroral oval, without considering the intricate details inside the auroral oval (e.g., Zhang and Paxton, 2008; Milan et al., 2009; Mitchell et al., 2013; Newell and Gjerloev, 2014). There are various websites (for the public) that forecast the auroral oval. Such forecasts are not only necessary if auroral scientists wish to share their understanding of the aurora, but they are also key to gaining a better understanding of space weather phenomena, including their effects on our technological society (e.g., review by Zheng and Rastaetter, 2016).

A major discovery has been that the auroral light of the auroral oval can be attributed to at least four types of particle precipitation. The associated auroras are now called quasi-static aurora, Alfvénic aurora, diffuse aurora and proton aurora (among other names), and it has been one of the central issues in the study of the aurora to determine the contributions of each type to the auroral oval. Section 3 is devoted to the Alfvénic impact on the auroral oval.

Other planets also have auroral ovals (Fig. 2). These provide excellent opportunities for comparisons with Earth's auroral oval to identify similarities and differences associated with the generation of the aurora (e.g., Mauk and Bagenal, 2012). However, the limited *in-situ* observations at other planets make it less feasible to directly probe a possibly associated Alfvénic oval. Instead, one can look for similarities in the auroral ovals of other planets, especially their dynamic behaviors, to make inferences about an underlying Alfvénic oval and compare it with that of Earth. Hence, what is reviewed here may also apply to the auroral ovals of other planets.

1.2. *Alfvénic oval*

The term "Alfvénic oval" evokes an analogy with the auroral oval, which was indeed the intention when it was first coined (Keiling et al., 2019b). Both ovals are related: they statistically cover the same regions (i.e., the auroral zone) around the magnetic poles; they can show similar, individual morphological features; and the auroral oval is partially caused by the Alfvénic oval. To reveal the Alfvénic oval, it is most convenient to map the Alfvén wave, measured in space, along magnetic field lines to the ionosphere. Poynting flux is the most common quantity to have been used for such mapping, because of its importance

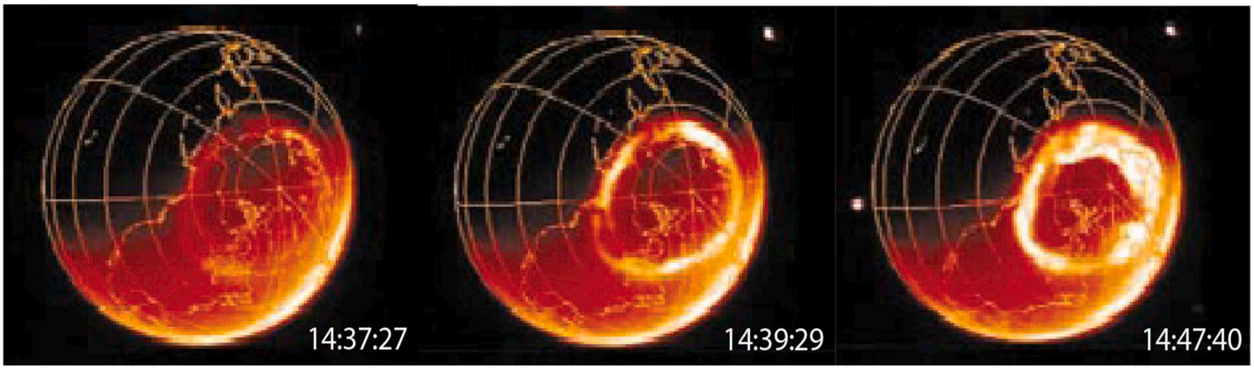

Fig. 1. Global view of the initial development of the aurora during the Bastille Day storm observed by the IMAGE spacecraft's Wideband Imaging Camera (from Burch, 2001).

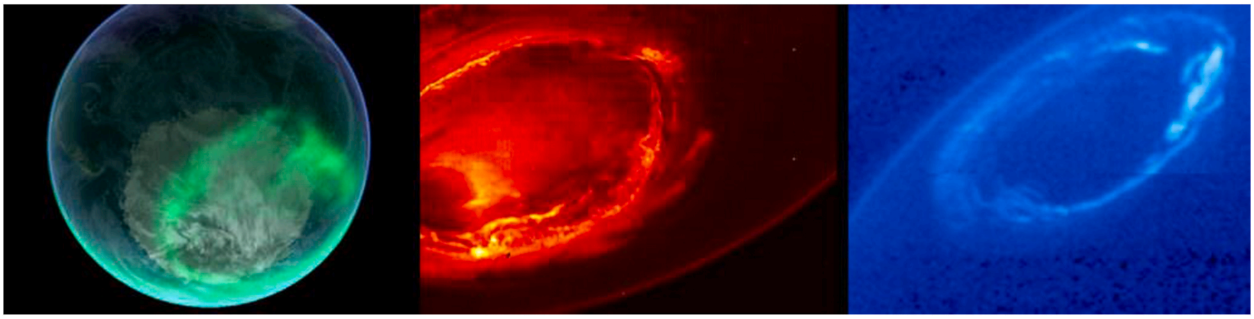

Fig. 2. Planetary auroral ovals: (left) Earth, (middle) Jupiter, and (right) Saturn. Credit: NASA.

but also because it provides directional information. Given the limited number of satellites and the enormous space to be covered, large databases collected over months or years are used. Fig. 3 illustrates a possible scenario, with a hypothetical orbital ellipsoid of a satellite, crossing different plasma regions of Earth's magnetosphere, as the satellite's orbit precesses throughout the year. Alfvén waves traveling through each of the grid cells are recorded, both those traveling toward and those traveling away from Earth. The colored regions on the ellipsoid illustrate regions through which more intense Alfvén waves travel. While this creates an oval-like structure in space, the shape of which varies significantly depending on where along the magnetic field lines the Alfvénic power is measured, the ionosphere is well suited as a region to compare the morphology and also the intensity of the Alfvénic oval, as recorded in different space regions and by different satellites. Thus, the studies reviewed here have mapped their measurements typically to an altitude of 100 km and displayed the data in the familiar ILAT-MLT format. It is this *mapped* Alfvénic oval that we refer to throughout this review. It is stressed that the Alfvénic distribution shown in Fig. 3 is only one possible "averaged" distribution (in fact, resembling that of Fig. 4b), obtained by processing (e.g., sorting) a large amount of data in each cell. Depending on the investigation at hand, one can extract different information, yielding different distributions, that is, different Alfvénic ovals. The multitude of such investigations is the topic of this entire review. Underlying each statistical Alfvénic oval are the many instantaneous Alfvénic ovals, which are as variable as the instantaneous, evolving auroral oval is.

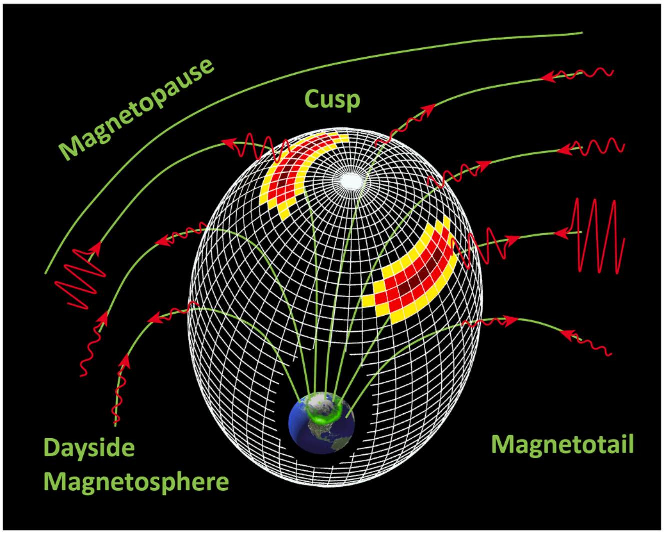

Fig. 3. (Modified from Keiling et al., 2019a) Hypothetical orbital ellipsoid of a polar-orbiting satellite crossing different plasma regions of Earth's magnetosphere. The colored grid cells represent regions through which larger-amplitude Alfvén waves (red, wavy lines) travel toward and away from the ionosphere, forming an "Alfvénic oval" in space. The hole in the ellipsoid reveals Earth with the aurora borealis. Green lines represent magnetic field lines.

The earliest studies showing the global aspect of Alfvénic oval morphology utilized the Astrid-2 microsatellite at 1000 km altitude (Ivchenko and Marklund, 2001), FAST at <4000 km altitude (Chaston et al., 2003), and Polar at 4–7 R_E (1 $R_E = 1$ Earth radius) geocentric distance (Keiling et al., 2003). A direct comparison of Alfvénic ovals, using Poynting flux, recorded at different altitudes was presented in Hatch et al. (2017), which demonstrates the following (Fig. 4a and b):

1. The same morphology below and above the AAR
2. Energy flux reduction from above to below the AAR
3. Perpendicular scale size change (from MHD to inertial) from above to below the AAR

(1) The dawn-dusk asymmetry is perhaps the most striking feature of both Alfvénic Poynting flux distributions, with enhancements post-noon and pre-midnight. Moreover, both oval-like bands of enhanced Alfvénic activity are shifted toward the nightside, in a similar fashion as the auroral oval. (2) There is significantly less Poynting flux at lower altitude (measured by FAST), suggesting that wave dissipation occurs at the expense of particle energization inside the AAR. Here it is important to note that all data (from FAST and Polar) were mapped, assuming no dissipation along the field lines below each satellite, onto the same reference altitude of 100 km, that is, ionospheric altitude. This allows comparison of values as if the background magnetic field strength was the same, which has an effect on the local value because of the "focusing" effect of the background magnetic field. (3) Whereas in panel (a), inertial Alfvén waves (IAW) were processed, panel (b) shows MHD waves. Together with observation (1), this suggests that there is a cascade from the MHD scale to the inertial scale, which can be explained by incorporating the effect of the AAR on the waves (see section 1.3).

While Alfvén waves have been intensely studied using simulations, most of this research has investigated the wave-particle interaction. However, simulations have also been successful in reproducing the global distribution of Alfvén waves. Zhang et al. (2012) conducted global MHD simulations, using one day of solar wind and IMF data as the inputs, and calculated the morphology of the wave Poynting flux (Fig. 4c), using the same frequency band and a similar "simulated" altitude as used in the Polar observations (Fig. 4b) for comparison, followed by mapping to the same ionospheric altitude of 100 km. (More details about this study are given in section 2.) The similarities with the observational distribution from Polar are striking with regard to several aspects, including dawn-dusk asymmetry, dayside-nightside asymmetry, and intensity variations. However, the latitudinal location of the enhanced Alfvénic region on the nightside differs somewhat between the simulation and the observations. The authors suggested mapping-related issues to explain this mismatch.

From Fig. 4b, the question might arise of whether it is justified to speak of an Alfvénic *oval*, given that the oval appears to be discontinued on the flanks. On the other hand, the question might also be considered futile, when we realize that the instantaneous aurora oval itself can be

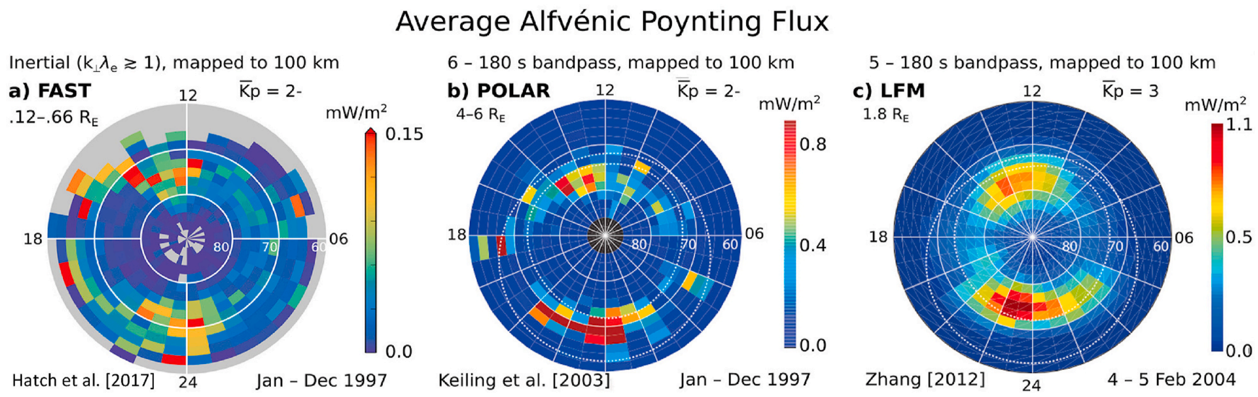

Fig. 4. Comparison of average Alfvénic Poynting flux distribution in the Northern Hemisphere (from Hatch et al., 2017). (a) IAW Poynting flux derived from one year of FAST observations (below the AAR). (b) MHD Alfvénic Poynting flux derived from one year of Polar observations (above the AAR). (c) MHD Alfvénic Poynting flux averaged over 24 h, derived from LFM (Lyon-Fedder-Mobarry) simulations. All values are mapped to 100 km altitude. (Note: All geomagnetic conditions are averaged over.)

"subvisual" in parts under, for example, conditions of a northward IMF (Akasofu, 1989). This discontinuous auroral oval has been discussed in Feldstein and Starkov (1967). Moreover, it is emphasized that the statistical representation of the three ovals in Fig. 4, averaged over all types of geomagnetic conditions, reveals nothing about the global, *instantaneous* Alfvénic morphology. By averaging over many thousand orbits, certain regions can appear less visible, even if Alfvénic activity is present everywhere but less frequent in certain regions. Thus, it can also be argued that in the statistical representations, adjusting the scale sensitivity would allow reduced activity in the "gap" region(s) to also be visible. Interestingly, Fig. 4c does show more clearly a "closed" Alfvénic oval, which is only averaged over 1 day, with weaker Alfvénic activity on the flanks. That the flanks are not always devoid or low on intense Alfvénic activity, but that it rather depends on geomagnetic activity level, will be shown in later sections, which review the dynamics of the oval under various geomagnetic conditions.

The question of a "closed" oval is related to the question of why a "band" of enhanced Alfvénic activity appears in the first place, given the prevalence of Alfvén waves in *all* regions of the magnetosphere (review by Keiling, 2009). This is because there are preferred regions in the magnetosphere for intense waves to occur, which indeed outline an oval when mapped onto the ionosphere. It has been reported that the Alfvénic power is 2–3 orders of magnitude larger in the plasma sheet (in particular the PSBL), compared to the Alfvénic power inside the lobe regions and the plasmasphere (Osaki et al., 1998; Keiling et al., 2005; Takada et al., 2006). This leads to an identifiable Alfvénic oval when this activity is mapped to the ionosphere. Excursions of Alfvénic activity to higher and lower latitudes (i.e., away from the statistical Alfvénic oval) occur (e.g., at 18 MLT in Fig. 4b). These can be explained by the expanding Alfvénic oval during more dynamic times, such as a geomagnetic storm in this case. On average, there are fewer such days throughout the year and thus they do not show in the statistical distribution (Fig. 4b), with a few exceptions. Below we show that excursions to lower latitudes occur for many MLT values, especially during storm times, which is analogous to the auroral oval, which expands to lower latitude during very active times (Chapman, 1957). Sorting the Alfvén wave data by various conditions reveals the different morphologies of the Alfvénic oval and is the topic of section 2.

For the remainder of this review, and for future usage by the space physics community, our definition of the Alfvénic oval is as follows. It is foremost the morphology of more intense Alfvén waves in the magnetosphere, which resembles an oval, similar in shape to and partially encompassing the auroral oval, when mapped onto the ionosphere (typically at 100 km, but that is not necessary). We define this "new" oval as the *primary* Alfvénic oval. It should be noted, though, that while Alfvén waves might be present at all times and everywhere, only the more intense Alfvén waves (one or more orders of magnitude larger than the neighboring waves) form the oval by our definition. Moreover, Alfvén waves accelerate electrons (sometimes called Alfvénic electrons), which also delineate an oval when mapped onto the ionosphere, as will be shown in later sections. This oval is here defined as the *secondary* Alfvénic oval. In our definition, both are considered the Alfvénic oval, while having a causal relationship. From the *secondary* Alfvénic oval, one can infer the existence of the driving *primary* Alfvénic oval. The interaction and exchange of energy between them implies that both *primary* and *secondary* ovals change along the flux tubes.

We can take this one step further. The Alfvénic oval can also refer to the visible part of the auroral oval that is powered by Alfvén waves. This is in analogy to Alfvénic aurora, that is, the aurora that is powered by Alfvén waves. This is the *tertiary* Alfvénic oval. Thus, starting with the original, *primary* Alfvénic oval (made up of waves), we have broadened the definition to include some of its effects, namely, the *secondary* and *tertiary* Alfvénic ovals. For presentation and better comparison, it is convenient to map all ovals onto a reference altitude, such as the ionosphere (typically 100 km), which has been done in many studies reviewed next. Fig. 5 illustrates the three layers of the Alfvénic oval to which we refer throughout this review. Note that the terms *primary* and *secondary* do not mean that one is physically located above the other (i.e., at a larger distance from Earth). Instead, it refers to the different component that is being measured or displayed, namely Alfvén waves and electrons. Thus, the secondary Alfvénic oval can also be measured at higher altitude than the primary Alfvénic oval. Furthermore, there can be several primary Alfvénic ovals along the field line, as there can be many secondary Alfvénic ovals, if measured at different locations.

Lastly, we assume that the reader is familiar with the basic physics of Alfvén waves, including the distinction between MHD regime and kinetic/inertial regime (or nondispersive and dispersive Alfvén waves, respectively). We also assume knowledge of the associated Poynting flux, which describes the important property of Alfvén waves to carry energy to other regions, and which can be converted into particle energy during dissipation processes. The Poynting flux also indicates the energy flow direction, which is not immediately apparent from the perturbation electric and magnetic fields of the Alfvén waves. If the reader is not familiar with any of these aspects, they are referred to the review by Keiling (2009), where the observational aspect is reviewed, including several techniques of how to detect Alfvén waves using space-based and ground-based measurements, while focusing on the MHD regime. In their review, the reader can also find a discussion on the calculation of the Poynting flux, which is not trivial and can lead to erroneous results. Detailed theoretical descriptions of inertial and kinetic Alfvén waves can be found in the review by Stasiewicz et al. (2000).

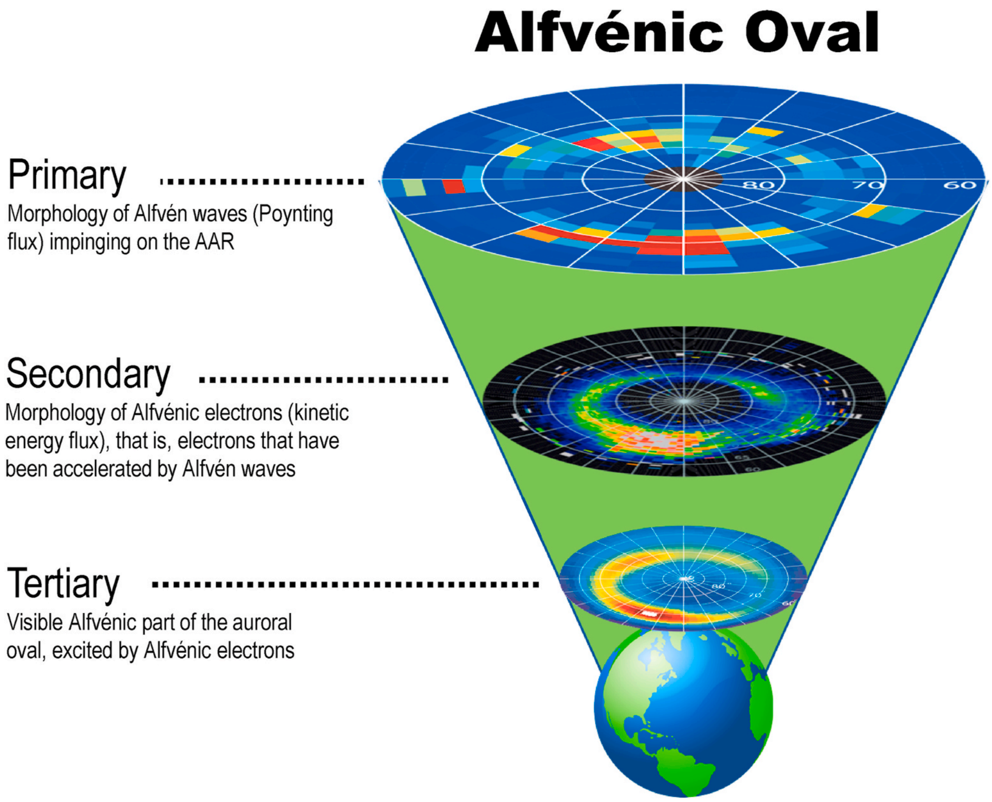

Fig. 5. Three layers of the Alfvénic oval (not to scale). Primary = Alfvén waves; secondary = Alfvénic electrons, which are electrons accelerated by Alfvén waves; tertiary = visible Alfvénic aurora (note: in this image, the entire aurora is shown, since no global image of the visible Alfvénic oval exists). The actual data shown in each layer (from Keiling et al., 2003; Newell et al., 2009; Liou et al., 1997, respectively) are repeated and described in other sections.

1.3. Auroral acceleration region

Energy transport and energy conversion are central concepts to our understanding of the coupled solar wind-magnetosphere-ionosphere system. The AAR is a key region in the coupling between the collisionless and tenuous magnetospheric plasma and the collisional and dense ionospheric plasma. It is a major region for energy conversion processes; in particular, inflowing electromagnetic energy is converted into the kinetic energy of electrons and ions—hence its name. The two forms of electromagnetic energy that dominate in this coupling scenario are quasi-static FACs and Alfvén waves (review by Mottez, 2016). Generated in various magnetospheric regions, some of their energy carried to the auroral zone is deposited inside the AAR *via* particle acceleration. We briefly discuss the AAR here, because it plays a special role that will help us with the analysis of the Alfvénic oval.

The physical altitude extent of the AAR is typically defined by the quasi-static structures shown in Fig. 6a. Based on these structures, the bulk of the AAR ranges between 1.5 R_E and 3.5 R_E geocentric (Mozer and Hull, 2001; review by Karlsson, 2012), but may extend to 5.5 R_E geocentric (Alm et al., 2015), measured from the center of the Earth. The exact location of Alfvénic acceleration is less defined (Fig. 6b) and can in fact occur well above and below the quasi-static AAR (e.g., Wygant

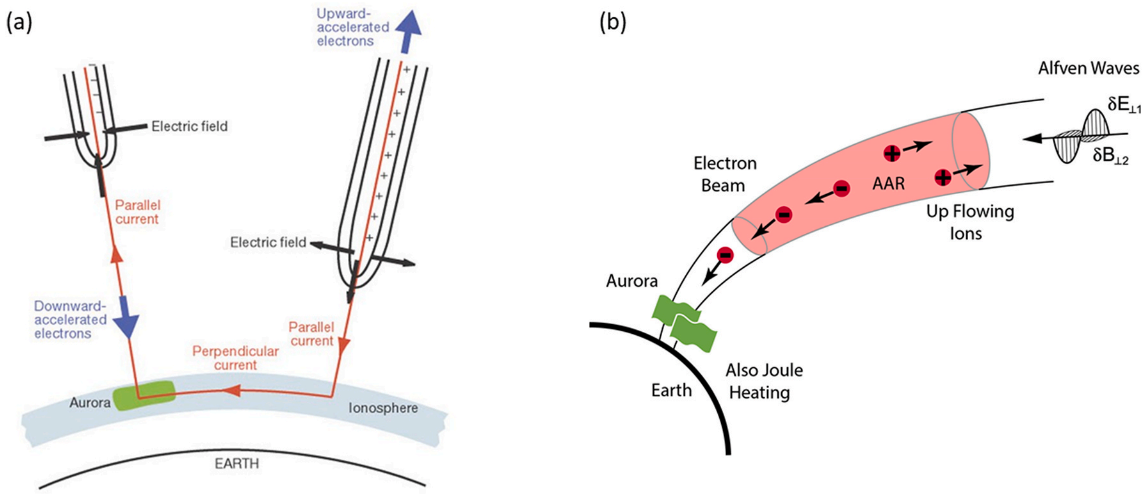

Fig. 6. Diagrams of acceleration mechanisms inside the auroral acceleration region (AAR). (a) Acceleration by quasi-static structures (Marklund et al., 2001). (b) Acceleration by Alfvén waves (after Wygant et al., 2000).

et al., 2002; Lynch et al., 2012). Chaston et al. (2003) argue, through the use of simulations and observations (from the FAST satellite which had an apogee of about 4000 km altitude), that most of the Alfvénic (auroral) electron acceleration occurs between 2 and 3 R_E geocentric. However, Janhunen et al. (2006) argue, using observations from the Polar satellite, which had an apogee of about 9 R_E (geocentric distance), that the majority occurs between 3.5 and 4.5 R_E (geocentric distance). This discrepancy should be resolved in future studies.

Alfvénic M-I coupling has been firmly established using case studies and theoretical arguments (review by Lotko, 2004). Alfvén waves interact with the AAR in several ways, including wave-particle interaction, wave reflection, and the formation of new structures (e.g., double layers). Moreover, an important phenomenon is the transformation from large-scale MHD to small-scale kinetic (or inertial) Alfvén waves along field lines inside the AAR, because the latter possess electric fields that are parallel to the ambient magnetic field, which can accelerate electrons that precipitate and cause auroras (Fig. 7). Alfvén waves are also thought to transversely accelerate ions, leading to their expulsion from the ionosphere (not included in Fig. 7). Chaston (2006) lists several proposed, but as yet unverified, mechanisms for the transverse-scale transformation, such as mode conversion from surface-mode Alfvén waves, refraction and phase mixing on density gradients, local instabilities associated with the current and flow shears in the wave and wave steepening, and ionospheric feedback within the ionospheric Alfvén resonator. These processes are not well understood, and ideally, require multipoint measurements inside the AAR to gain a better understanding. Comprising four satellites in close formation, the Cluster mission has provided much-needed insight into the workings of the AAR from a multipoint viewpoint (review by Forsyth and Fazakerley, 2012; Forsyth et al., 2014; Alm et al., 2015; Hull et al., 2016), but clearly more work and additional dedicated multi-satellite missions are required.

To understand the action of the AAR on Alfvén waves, a useful approach has been to conduct conjugate studies that relate satellite observations along a fluxtube (at approximately the same time) from a location near the topside of the AAR and one near (or below) the bottom side of the AAR. So far, there are only a few studies that have done such conjugate comparisons for individual events, where the conversion of electromagnetic energy to particle energy, while reducing the wave energy, was demonstrated (e.g., Vaivads et al., 2003; Dombeck et al., 2005; Chaston et al., 2005). Instead of measuring the electron precipitation directly, the kinetic energy flux of the auroral electrons has been inferred from auroral images and has then been compared with conjugate high-altitude Alfvénic Poynting fluxes (e.g., Wygant et al., 2000; Keiling et al., 2002). To investigate a large region, such as the nightside auroral zone or the entire hemisphere, yearly averages of global morphology and total power of Alfvén waves and auroral electrons from different satellites have been compared (references provided throughout this review). All these studies provide important information on the energy balance between the topside and bottom side of the AAR, while leaving out the details inside the AAR (i.e., treating the AAR as a black box). Because in this review the focus lies on the global Alfvénic oval, the statistical approach is of relevance here.

Knowledge of the secondary Alfvénic oval, as defined in section 1.2, rests on our ability to identify electrons that have been accelerated by Alfvén waves (i.e., Alfvénic electrons). The fact that specific electron properties are associated with different acceleration mechanisms allows us to achieve this goal. In the case of Alfvénic acceleration, it has been shown experimentally that kinetic Alfvén waves lead to electron precipitation with a broad energy range (e.g., Chaston et al., 2003), and test particle simulations have confirmed this description (e.g., Kletzing and Hu, 2001; Chaston et al., 2002). While some skepticism has been voiced (Dombeck et al., 2018), it is still a reasonable description and is currently our best approximation.

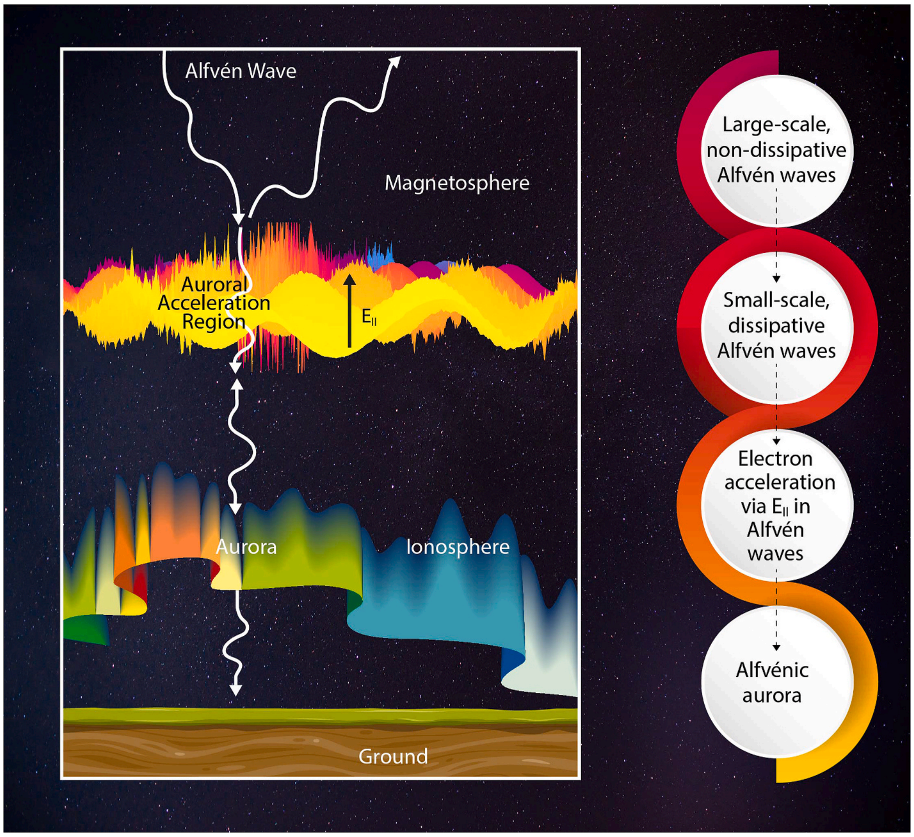

Fig. 7. Alfvénic M-I coupling scenario with scale cascade, field-aligned electric field, wave-particle interaction inside the auroral acceleration region, and auroral excitation. Inset on the left was modeled after a figure in Fedorov et al. (2004).

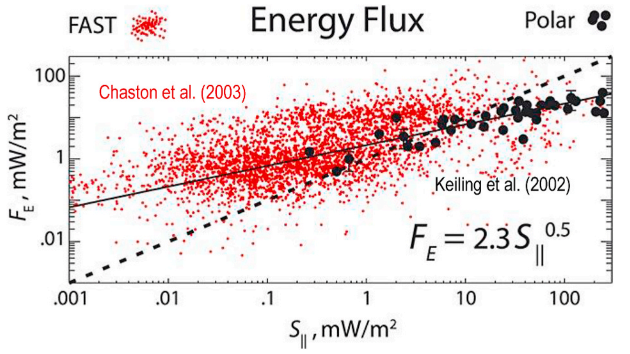

Fig. 8. (From Zhang et al., 2015) Precipitating electron energy flux, F_E, from FAST electron measurements (Chaston et al., 2003) and inferred from Polar UVI images (Keiling et al., 2002) versus simultaneously measured downward Poynting flux ($S_{||}$) in the 0.2–20 Hz passband from FAST at altitudes of 2000–4000 km and in the 6–180 s passband from Polar at 4–6 R_E geocentric distance. All fluxes are mapped to a reference altitude of 100 km. The dashed line is $F_E = S_{||}$ and the solid line indicates the approximate (visual) regression based on the Polar data.

It is also important to acknowledge that not all of the high-altitude Alfvénic Poynting flux entering the AAR is converted into the kinetic energy of precipitating (auroral) electrons. For example, some of the wave energy will go into Joule heating, upwardly-accelerated electrons and ion heating, or will be reflected back into the magnetosphere. Therefore, an important question relates to how much of the incoming Alfvénic Poynting flux can be converted into kinetic energy of electrons. This question has been addressed from theoretical and numerical viewpoints by investigating the efficiency of the energy conversion mechanism (Chaston et al., 2002; Pilipenko et al., 2004; Lysak and Song, 2005; Watt et al., 2005; and Song and Lysak, 2006). Two empirical approaches have provided mathematical relationships for the energy transfer from Alfvén waves ($S_{||}$) to electrons (F_E) inside the AAR, one for individual events and one for the global oval (subscript "e" for individual events and "g" for global statistics were added to distinguish the quantities):

$$F_{E,e} = 2.3\,(S_{||,e})^{0.5} \tag{1}$$

$$F_{E,g} = 0.56\,S_{||,g} \tag{2}$$

Equation (1) was obtained by Zhang et al. (2015) from data measured by the Polar satellite (Keiling et al., 2002). It relates the high-altitude (above the AAR) Poynting flux, $S_{||,e}$, of an individual event to the conjugate kinetic energy flux of precipitating electrons, $F_{E,e}$, at ionospheric altitude (100 km), presumably accelerated by the Alfvén waves. The equation accounts for the partial absorption of wave energy by electrons inside the AAR, with an absorption efficiency that is dependent on the amplitude of the incoming Alfvén waves. Fig. 8 shows the Polar dataset together with data from FAST (Chaston et al., 2003). The solid line is the approximate regression line (drawn visually through the Polar dataset) used to obtain equation (1). This figure also illustrates that above the AAR, the Poynting flux is larger than the corresponding low-altitude electron energy flux (black dots below the dashed line), thus being sufficient for energization, while below the AAR, most energy flux is contained in the electrons and the remaining Poynting flux is much lower (red dots above the dashed line).

Equation (2) was obtained by Keiling et al. (2019b) from data measured by the DMSP (Newell and Gjerloev, 2011) and Polar (Keiling et al., 2019b) satellites. This time, it relates the high-altitude, global Alfvénic power, $S_{||,g}$, to the global kinetic energy flux of precipitating electrons, $F_{E,g}$, both integrated over the entire nightside auroral zone. While the equation accounts for the partial absorption of wave energy by electrons inside the AAR, it does not differentiate between different wave amplitudes, and thus represents an average value. This equation suggests a total Alfvén wave absorption by wave-particle interactions inside the AAR of 56%. This absorption efficiency can be compared with the estimates based on theoretical considerations, which provide comparable values (e.g., Chaston et al., 2002; Pilipenko et al., 2004). Keiling et al. (2019b) also estimated a global Alfvén wave reflection of 33% (upper limit), and an excess wave power of 11% (lower limit), available for other energy conversion processes, such as Joule heating and Alfvénic ion outflow.

Both equations are important, because they allow one to ignore the details of wave-particle interaction inside the AAR. They both take Poynting flux values from above the AAR and make projections about Alfvénic electrons below the AAR. Strictly speaking, both equations were derived from nightside auroral zone data only and are therefore only valid in this region. It is also important to note that equation (2) applies to the global relationship between Alfvén wave power and Alfvénic electron energy flux and not necessarily to individual events, for which equation (1) offers the appropriate relationship. This clearly manifests in the different slopes. While equation (2) has a constant slope, equation (1) has a variable slope.

In Fig. 9, the application of both equations is graphically illustrated. We tested both flowcharts by applying them to 6 years of Polar data. Following the upper flowchart, we first generated the global distribution map of Alfvén waves above the AAR and then mapped to ionospheric altitude. Integration over the nightside yields a total power of 1.56 GW, which is the total inflowing Alfvén wave power. Then, equation (2), which incorporates the wave-particle interaction, yields a global, precipitating Alfvénic electron power of 0.87 GW. Following the lower flowchart, we first applied equation (1) to individual events recorded above the AAR to generate the global distribution map of Alfvénic electrons at ionospheric altitude. This equation contains the wave-particle interaction. Since equation (1) becomes non-physical for $S_{||,e}$, $<$ 5.2 mW/m^2 (where the electron flux is greater than the driving Poynting flux), we only used it for values of $S_{||,e}$, $>$ 5.2 mW/m^2. For values of $S_{||,e}$, $<$ 5.2 mW/m^2, we used $S_{||,e}$, $= F_{E,e}$, representing a 100% energy transfer, which is unrealistic but nonetheless used as an approximation. After integration over the nightside, we obtained a total, precipitating electron power of 0.98 GW, which is in reasonable agreement with the value of 0.87 GW obtained from the upper flowchart. In the remainder of this review, additional examples of both equations are given.

2. Global dependences

The Alfvénic oval has been probed *in situ* through recording the electric and magnetic field perturbations of the Alfvén waves (primary Alfvénic oval) and through recording the Alfvénic electrons (secondary Alfvénic oval), which are consequences of wave-particle interaction. Both types of Alfvénic ovals were defined in section 1.2. Many studies have reported their results in terms of energy flux for both waves and electrons, which allows direct comparison between the primary and secondary ovals. Since extremely large regions in space are involved, we must rely on statistical data recorded during hundreds to thousands of satellite orbits, together with simulations, to help us understand the dynamics of the *global* Alfvénic oval. It is again emphasized that "global" (here and throughout the review) refers to the entire hemisphere or, in a few cases, to the nightside auroral zone. While in this section the primary and secondary Alfvénic ovals are reviewed, the tertiary Alfvénic oval is specifically addressed in section 3.

While in principle the Alfvénic oval (primary and secondary) can be observed anywhere along the magnetic field lines, two of the most meaningful and convenient locations are below the AAR and above the AAR. The comparison of results from both regions allows for the assessment of the effect of the AAR on the Alfvénic oval, while treating the AAR as a black box (cf. section 1.3). Even though there is no temporal conjugacy in the statistical data comparison, the "time-averaged" results provide remarkable consistency, as shown in this section, which

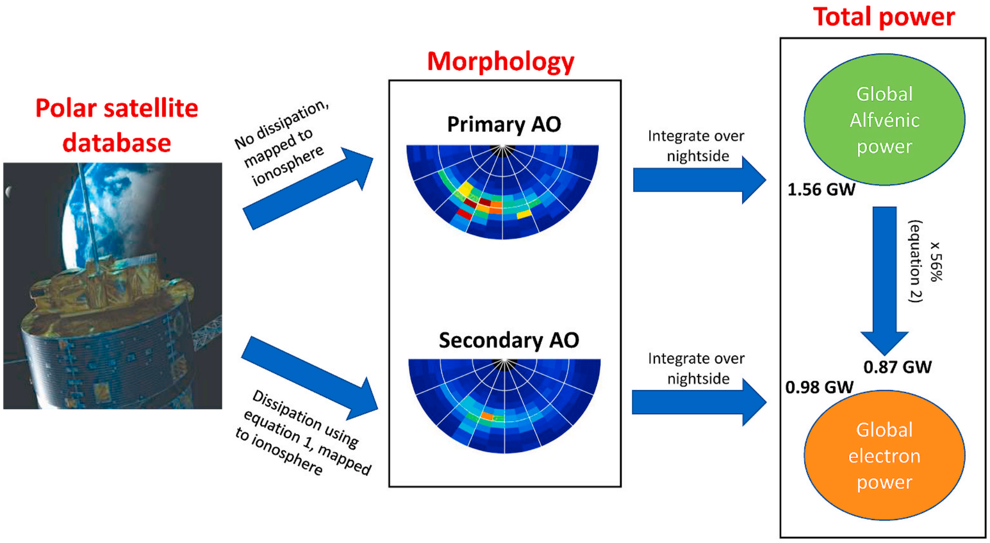

Fig. 9. Flowchart showing two ways of calculating the global, precipitating Alfvénic electron power from Alfvén wave data recorded above the AAR over the nightside auroral zone. AO stands for Alfvénic oval. Both start out with the same database of electric and magnetic field data from the Polar satellite, which are the fundamental quantities of an Alfvén wave. Here we show Polar, but any satellite can be used as long as the data are collected above the AAR. See text for further explanation.

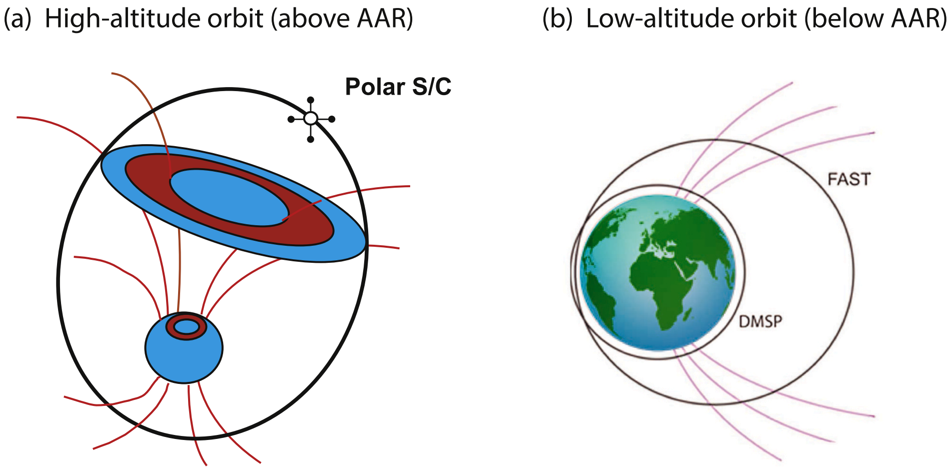

Fig. 10. The generic setup to investigate the dynamics of the Alfvénic oval: (a) Polar's orbit (1.8 R_E perigee, 9 R_E apogee). The blue sphere is Earth. (from Keiling et al., 2003). (b) Orbits of FAST (<4000 km) and DMSP (~850 km) (modified from Dombeck et al., 2005).

yields important insight into the global dynamics of the Alfvénic oval. Fig. 10 illustrates the generic setup, using the Polar satellite (panel a), and the FAST and DMSP satellites (panel b). Most statistical studies reviewed herein utilized these satellites. The altitude range of FAST and DMSP covers the lower end of the AAR and below, and thus, it is a region that should indeed experience some of the effects of higher-altitude Alfvén waves observed at Polar, located above the quasi-static AAR in parts of its orbit. The reader is referred to the relevant papers for each spacecraft for detailed descriptions about the instruments.

Furthermore, global simulations have reproduced the observed Alfvénic oval, while also providing information on the origin of the Alfvén waves and other parameters. Simulations allow for "controlled" virtual experiments to complement the observations, after verification that they actually produce reasonable results. A successful scheme, used in a series of studies (Zhang et al., 2012, 2014, 2015) and reviewed below, is illustrated in Fig. 11. The Alfvénic oval is generated using the Lyon-Fedder-Mobarry (LFM) global magnetosphere simulation code (Lyon et al., 2004), together with the Magnetosphere Ionosphere Coupler/Solver (MIX) module (Merkin and Lyon, 2010). Later, an electron precipitation model was added, but is not shown in this figure (see Zhang et al., 2015). The simulated primary Alfvénic oval is processed in the same way as that in the Polar satellite-based studies (e.g., Keiling et al., 2003), which allows for easier comparison of the observation and simulation results, as also reviewed in this section.

2.1. AE dependence

The auroral electrojet (*AE*) index is a well-known measure of auroral zone activity (Davis and Sugiura, 1966). For example, the aurora (e.g., Meng and Liou, 2002) and electron precipitation (Ahn et al., 1983) are correlated with changes in *AE*. *AE* has been shown to also correlate with Alfvén wave activity and Alfvénic electron precipitation (reviewed herein). The *AE* index also captures substorm activity, which is known to cause the generation of energetic Alfvén waves in the magnetotail (Maynard et al., 1996; Keiling et al., 2000). Substorm activity is specifically dealt with in section 2.2, whereas here we explore the general relationship between the spatial distribution and total electromagnetic power of the Alfvénic oval and *AE*. It turns out that there is a remarkably simple relationship between power and *AE*, namely, linear.

Fig. 12a shows the Alfvénic oval morphology for different *AE* ranges,

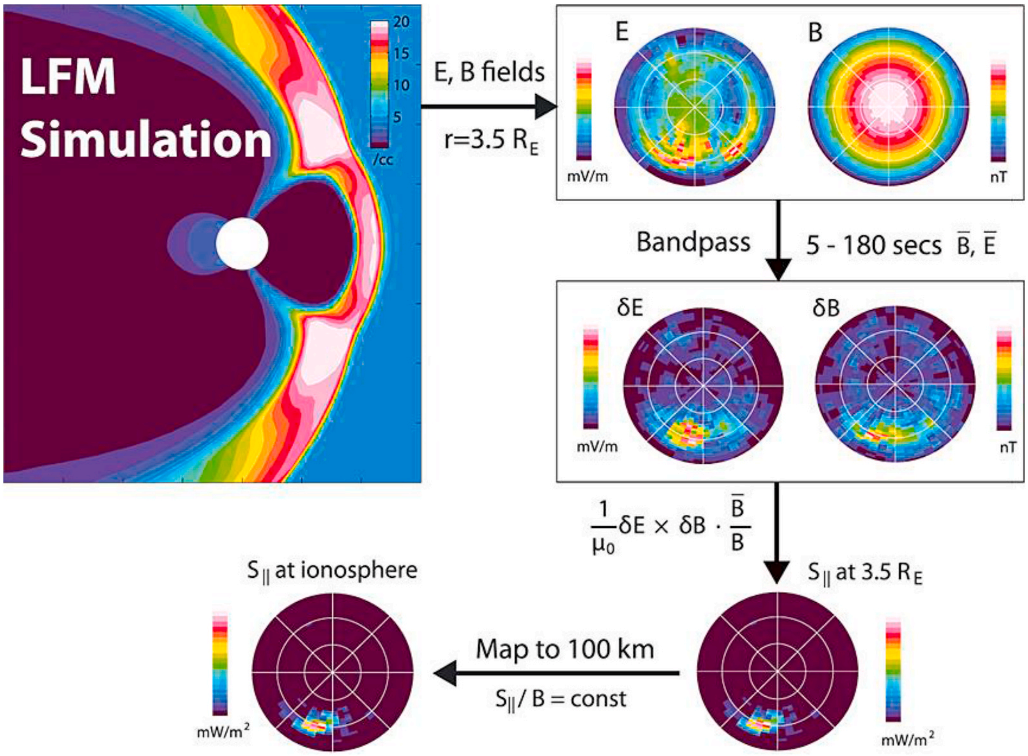

Fig. 11. Simulation setup of Alfvénic Poynting flux calculation from Zhang et al. (2014). The algorithm resolves electromagnetic waves in the range of 5–180 s. The simulated Alfvénic Poynting flux recorded on grid cells at the r = 3.5 R_E surface is then mapped to a reference altitude of 100 km along magnetic field lines such that $S_\parallel/B$ = constant.

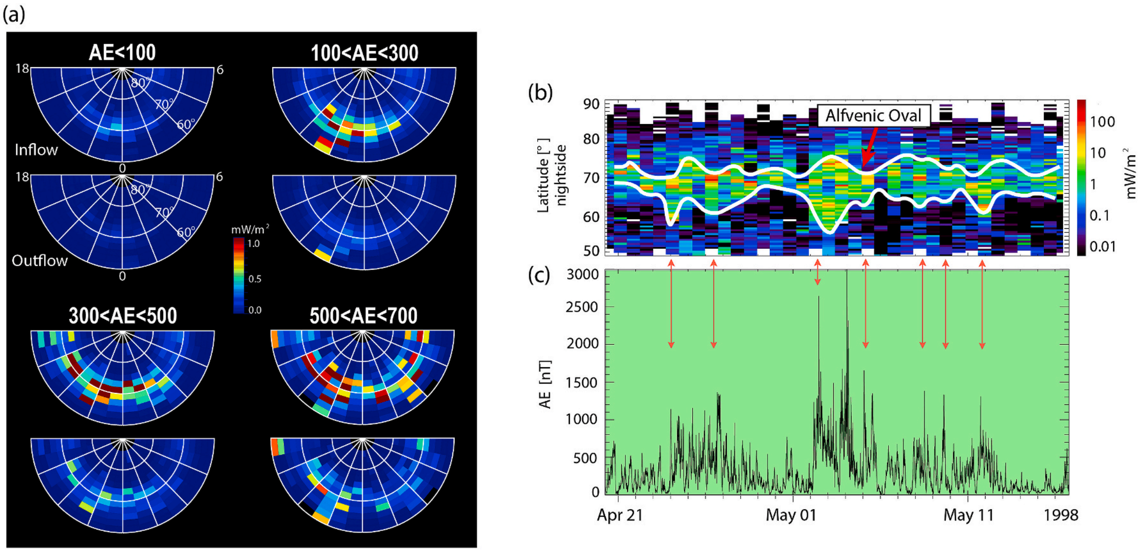

Fig. 12. (From Keiling et al., 2019b) (a) Morphology (MLT-ILAT format) of *in-situ* Poynting flux in the 6–180 s passband for the period from 1997 to 2002 for the nightside region, using Polar satellite data between 4 and 7 R_E. Each panel only contains Poynting fluxes during periods of activity indicated by the *AE* range (nT) at the top of each panel. The top and bottom in each panel show the average wave Poynting flux flowing into the AAR and out of the AAR, respectively. (b) Tracing Poynting flux along Polar's orbit during a period of 27 days. Peak values of Poynting flux are binned by 0.5° magnetic latitude (y axis) versus days (x axis) and mapped to ionospheric altitude. Each column represents a section of Polar's orbit within 50–90° magnetic latitude. Only values obtained when Polar was on the nightside are included. (c) *AE* index versus time. The red vertical lines with arrowheads mark expansion to lower latitudes of intense Poynting flux (panel b) in relation to *AE* peaks.

viewed from above the north pole. Here, only the nightside is shown, since *AE* is mostly an indicator for nightside activity. It can be seen that the regions of enhanced Poynting flux grow in longitude and latitude with increasing *AE*. Both inflow and outflow are shown, which refer to Poynting flux flowing into and out of the AAR at its topside, respectively. While for $AE < 100$ nT, hardly any Alfvén wave power is observed (light blue), the oval is clearly visible for 100 nT $< AE <$ 300 nT (light blue, yellow, orange and red), followed by an expansion of more intense regions (yellow and red) in longitude (for 300 nT $< AE <$ 500 nT) and also latitude (for 500 nT $< AE <$ 700 nT). While this general trend applies to both inflow and outflow, the intensities are significantly smaller for the outflow.

This latitudinal expansion and shrinkage of the Alfvénic oval can also be seen in Fig. 12b, which shows Poynting flux along Polar's orbit during a period of 27 days. The white lines approximately delineate the equatorward and poleward boundary of enhanced Poynting flux (>1 mW/m^2). When compared with the *AE* index (Fig. 12c), there is clearly a correlation with the width of this "Alfvénic band", as it extends to lower latitudes for larger *AE* values, which is pointed out by several arrows.

Each distribution in Fig. 12a possesses a global power value (in GW). Plotted in Fig. 13, the global “net” power (i.e., inflow minus outflow power) exhibits a linear relationship with *AE*. The green data points, also showing a linear trend, are from an analysis of precipitating Alfvénic electrons below the AAR (Newell and Gjerloev, 2011). The resulting equations are:

Newell and Gjerloev (2011):

$$FE\ [\mathrm{GW}] = 0.005\ \mathrm{GW/nT} \cdot AE\ [\mathrm{nT}] + 0.1\ \mathrm{GW} \tag{3}$$

Keiling et al. (2019b):

$$AW_{net}\ [\mathrm{GW}] = 0.006\ \mathrm{GW/nT} \cdot AE\ [\mathrm{nT}] + 0.2\ \mathrm{GW} \tag{4}$$

The reader is reminded that both datasets are related to the primary and secondary Alfvénic ovals (*cf*. Fig. 5), as defined in section 1.2. The net Alfvén wave power is clearly larger, which is to be expected, since it is assumed that the Alfvénic electrons are accelerated by the waves. The net power accounts for the fact that a portion of incident Alfvén waves are reflected back from below. However, it is also cautioned that not all of the outflowing power is in fact reflected wave power, but instead might be due to some wave generation occurring at lower altitude, particularly inside the ionosphere (see Keiling et al., 2019b, for more discussion).

These statistical linear relationships allow for the estimation of the “instantaneous” global Alfvén wave power and global Alfvénic electron power, when no such instantaneous measurements are even possible. For example, one can convert the time-varying *AE* index for an event directly into variations of global Alfvén wave power impinging on the AAR and precipitating global electron energy flux. An illustration is given in section 3.1. Similarly, solar wind/IMF parameters have been shown to control the *AE* index and mathematical equations have been developed (Akasofu et al., 1981, 2001). Combining such equations with the here-reported equations, Alfvén wave power and electron energy flux can thus be inferred directly from the solar wind/IMF parameters.

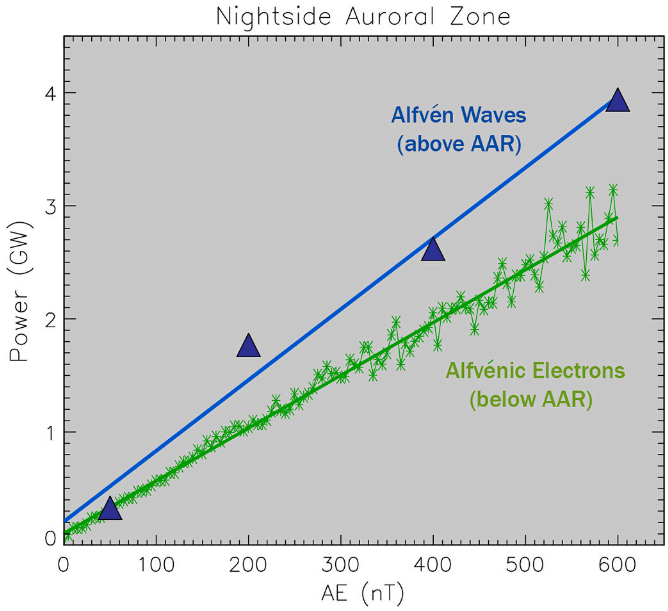

Fig. 13. (From Keiling et al., 2019b) Comparison of “net” inflowing Alfvén wave power, AW_{net}, above the AAR and Alfvénic electron precipitation power, *FE*, below the AAR. The regression line for the net Alfvén wave power (blue) is AW_{net} [GW] = 0.006 GW/nT · *AE* [nT] + 0.2 GW. The Alfvénic electron data (green) are reproduced from Newell and Gjerloev (2011). The regression line (green) is *FE* [GW] = 0.005 GW/nT · *AE* [nT] + 0.1 GW.

2.2. Substorm dependence

One of the most studied aspects of magnetospheric dynamics is the substorm. Its auroral signature is nothing short of spectacular, both as seen from the ground and space. The auroral development of a substorm, shown in Fig. 14, can last for several hours. The recognition that it obeys a fairly regular pattern was a great achievement, first inferred from ground data (Akasofu, 1964), which ultimately allows us to study this phenomenon. While a plethora of phenomena accompanies the auroral development, we focus again on the Alfvénic oval, which also shows a regular pattern and is in fact also partly responsible for the auroral pattern (more in section 3).

The onset of substorms is associated with burst-like enhancements of Alfvén wave power throughout the magnetotail (e.g., Maynard et al., 1996; Takahashi et al., 1988; Osaki et al., 1998; Keiling et al., 2000; Mende et al., 2003; Hull et al., 2016). The substorm association of the Alfvénic oval has been demonstrated in several statistical studies (Chaston et al., 2007; Lee et al., 2010; Newell et al., 2010; Wing et al., 2013; Keiling et al., 2020). Again, using the MLT-ILAT format, there is a clear and repeatable spatial pattern that can be observed in relation to substorm onset (Fig. 15): very little Alfvénic activity and total power before onset, and a sharp increase thereafter (Wing et al., 2013). The data show the energy flux of Alfvénic electrons recorded below the AAR (from DMSP), sorted by time in relation to substorm onset ($\Delta t = 0$ min). Many thousand substorms are combined in this figure. A comparison with Fig. 14 shows that the spatial distribution of the Alfvénic electron energy flux is similar to that of the auroral bulge, which is the most dynamic structure during the development of a substorm. While Fig. 14 shows instantaneous images, the same cannot be done for the Alfvénic oval. Nevertheless, the averaged maps in Fig. 15 clearly support the idea that Alfvén waves play a significant role in the generation of the auroral bulge.

These low-altitude (below the AAR) results can be compared with high-altitude (above the AAR) observations of Alfvén wave power. The corresponding global Alfvénic oval distribution is shown in Keiling et al. (2020), which is very similar to Fig. 15a. The integrated power values of individual global maps (nightside only) are plotted in a time series format for comparison in Fig. 15b, showing both low-altitude, total

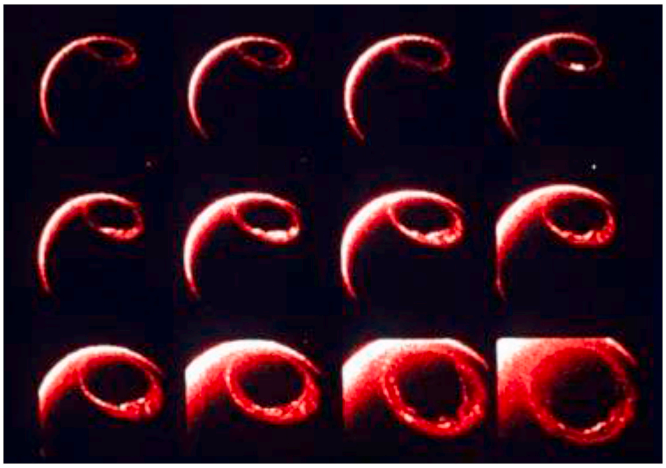

Fig. 14. This image shows the expanding auroral oval during a substorm (courtesy of L. Frank).

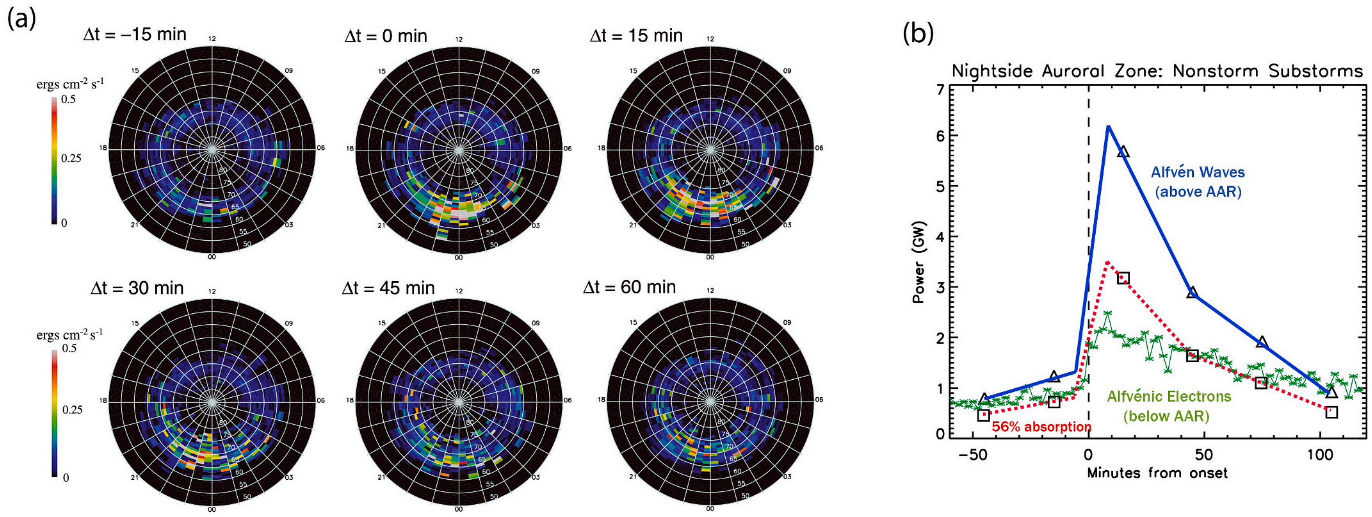

Fig. 15. Temporal evolution of the statistical Alfvénic oval during substorms. (a) (From Wing et al., 2013) Broadband/wave aurora electron energy flux (DMSP satellite) from 15 min before to 1 h after the substorm onset. Each map shows the median energy flux over a 15-min interval centered at the time labeled. The substorm onset occurs at $\Delta t = 0$ min. **(b)** (Modified from Keiling et al., 2020) Total inflowing Alfvén wave power (blue) recorded above the AAR (Polar satellite) in relation to substorm onset, together with Alfvénic electron precipitation power (green) below the AAR (DMSP satellite). The dotted red line accounts for 56% absorption of the Alfvén wave power (see equation (2)).

Alfvénic electron power and high-altitude, total Alfvén wave power. It is worth noting that data for nonstorm/isolated substorms are plotted. A comparison of nonisolated/recurrent substorms can be found in Keiling et al. (2020). While the blue solid line and red dashed line are derived from Alfvén wave data, the green data are derived from electron data. The red dashed line is an estimate of the Alfvénic absorption by electrons, obtained using equation (2) from section 1.2 (Keiling et al., 2019b). The most visible feature is the sharp rise of both Alfvén wave power and electron power during the expansion phase (starting at around $\Delta t = 0$), followed by a gradual decay to pre-onset values within about 2 h later. While there are some minor methodological differences between the DMSP and Polar statistics (summarized in Keiling et al., 2020), there is good agreement to support the Alfvénic driving scenario.

As is well known, the substorm expansion is the most dynamic phase during the substorm cycle, when rapid changes in the magnetotail, such as reconfiguration from a stretched tail-like magnetic field to a more dipolar magnetic field, enhanced tail reconnection and increased fast plasma flows occur. This active period is thus especially prone to Alfvén wave generation in the magnetotail, which is confirmed in the temporal evolution of the global Alfvén wave power reviewed here, with the largest peak power and power rise observed after onset. While the auroral bulge is the most dynamic structure of the substorm aurora, it has also been reported that the global Alfvénic substorm aurora is the most dynamic auroral type compared to the other auroral types, even if the absolute power values are smaller (Newell et al., 2009). This indeed links the auroral bulge strongly to the Alfvénic aurora; the extent of which is reviewed in section 3. Further support comes from the observation that about 50% of the Alfvén wave power over the entire nightside auroral zone is collocated with the auroral bulge region during the expansion phase (Keiling et al., 2020).

2.3. Storm dependence

Geomagnetic storms are periods of drastically increased energy input into geospace, followed by enhanced energy transfer and deposition within it (review by Gonzales et al., 1994). Since the nineteenth century, "grand" auroras—more global, more intense—have been related to increased disturbances in the geomagnetic field (e.g., Perry, 1880). While they can last for days, they also contain temporal structures of much smaller time scales. As shown in Fig. 1, the aurora "explodes" within only 10 min to cover the entire auroral oval. Such time scales are ideal for Alfvén wave activity. In fact, it has been demonstrated that Alfvén waves are an important component of geomagnetic storms and associated energy flow into the AAR. Several statistical studies have investigated the global impact of geomagnetic storms on the Alfvénic oval, which are reviewed in this section.

Hatch et al. (2018) investigated the global spatial distributions of power carried by inertial Alfvén waves (IAW) and Alfvénic electron energy flux using the FAST satellite at altitudes below 4000 km, while Keiling et al. (2019a) utilized the Polar satellite at geocentric distances between 4 and 7 R_E, that is, mostly above the AAR, to investigate MHD Alfvén waves. While the former study used about 3 years of data, the latter study used 6 years of data. Fig. 16 shows the corresponding Alfvénic ovals, both for Alfvén waves and Alfvénic electrons, during nonstorm periods and storm periods. (We remind the reader that these distributions represent two of the three layers of Fig. 5.) It is apparent that there are striking differences between the nonstorm and storm distributions at Polar (panel a) and FAST (panel b). Overall, the global "band" of more intense Alfvén wave/electron activity is significantly increased in size during storm periods compared to nonstorm periods. Concurrently, the various integrated, hemispheric power values (number in lower-left corner of each distribution) are significantly larger during storm periods compared to nonstorm periods (e.g., panel (a) shows 2.6 GW for nonstorm and 8.6 GW for storms).

Alternatively, when comparing the spatial distributions from higher altitude (above the AAR) with those at lower altitude (below the AAR), either during nonstorm or storm period, there is morphological similarity to suggest that there is a causal connection. For example, comparing the nonstorm distributions of panel (a) and panel (b), it is apparent that there are slightly enhanced regions of Alfvénic activity and electron precipitation around noon and midnight. Note that the scale for the FAST data is logarithmic, which partially explains the appearance of a wider oval, compared to the linear scale for the Polar data. Another reason for the wider oval at FAST might be that after the MHD Alfvén waves convert into IAWs, the waves have a perpendicular velocity component that could latitudinally broaden the oval, which would indirectly also apply to the electrons, being accelerated by the IAW. Similarly, the distributions during storm periods are very similar at both altitudes (panels a and b), in that they show latitudinally and longitudinally broadened intense Alfvénic activity.

A causal connection also requires that the total wave power flowing into the AAR is larger (or at least equal) to the combined wave and

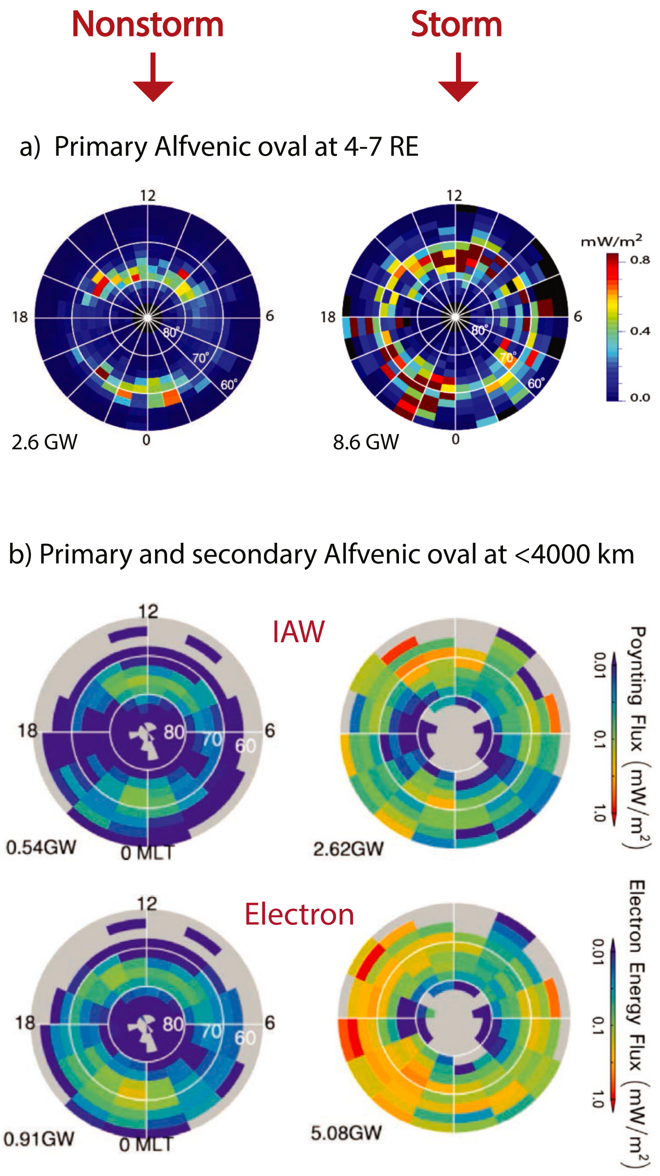

Fig. 16. Comparison of the morphology of the primary and secondary Alfvénic ovals during nonstorm and storm periods: (a) from Keiling et al. (2019a), using Polar data recorded above the AAR; (b) from Hatch et al. (2018), using FAST data mostly below the AAR. Note that the storm period distribution in (a) contains events occurring during both main phase and recovery phase, whereas that in (b) only contains events occurring during the main phase.

particle power flowing out of the AAR at the bottom. This is indeed the case for both nonstorm and storm periods (e.g., 2.6 GW versus 0.54 and 0.91 GW for nonstorm in Fig. 16). However, one also has to account for partial wave reflection of the inflowing waves, which reduces the total net inflow of wave power available for the low-altitude acceleration processes. This additional analysis was done for nonstorm periods, the main phase and the recovery phase of storms, the results of which are summarized in Table 1. The listed values (in GW) are global, hemispheric energy rates calculated from the same data shown in Fig. 16, by further sorting the storm distributions (Hatch et al., 2018; Keiling et al., 2019a). The net inflow of wave power (third row for Polar data) can be compared with the net energy absorption by IAWs and Alfvénic electrons (third row for FAST data). Only in the case of nonstorm periods appears the wave energy flux to be sufficient, which is consistent with the scenario that the high-altitude Alfvén waves power the low-altitude processes. Possible physical reasons for the “missing” energy flux during the two storm phases are: (a) only MHD waves were considered at Polar’s altitude and KAW at Polar might also contribute; (b) it is not certain that all of the upflowing Alfvén wave power recorded at Polar represent reflected wave power, because it is known that especially during storms, Alfvén waves can be generated in the ionosphere by other energy sources (e.g., Nishimura et al., 2010), which would increase the net deposition value at Polar. While this attempt to combine various power values for the energy balance in Alfvénic M-I coupling during geomagnetic storms provides us with some insight, it remains incomplete because of some deficiencies. The interested reader is referred to Keiling et al. (2019a) for more discussion on this, and to section 4 for some additional discussion as well.

The comparison of primary and secondary Alfvénic ovals during storms is also suited to test equation (2) from section 1.3 (*cf.* Fig. 9), which allows calculating the energy absorption by electrons from the total inflowing Alfvénic power. From Table 1, we find that the global inflowing Alfvénic power during the main phase is 10.05 GW. Applying 56% absorption efficiency, the global Alfvénic electron power is 5.62 GW. In comparison, from low-altitude FAST measurements, the global Alfvénic electron power during the main phase is estimated to be 5.08 GW (Table 1). Both values are very similar. It is noted that FAST data were not involved in deriving equation (2); thus, this comparison adds

Table 1
Comparison of global powers for the Northern Polar Region (from Keiling et al., 2019a).

Satellite	Nonstorm	Main phase	Recovery phase
Polar (above AAR)[a]			
Alfvén wave$_{\mathrm{down}}$ (GW)	2.59	10.05	6.29
Alfvén wave$_{\mathrm{up}}$ (GW)	0.67	4.07	2.62
Net deposition[b] (GW)	1.92	5.98	3.67
FAST (below AAR)[c]			
Alfvén wave (GW)	0.54	2.62	1.75
Electron precipitation (GW)	0.91	5.08	4.27
Net deposition[d] (GW)	1.45	7.70	6.02

[a] Polar study period: January 1997 to December 2002 (from Keiling et al., 2019a).

[b] Net deposition at Polar is not necessarily the true deposition below the auroral acceleration region (AAR). See text for explanation.

[c] FAST study period: October 1996 to November 1999 (from Hatch et al., 2018).

[d] Calculated under the assumption that all Alfvén wave power at FAST flows toward the ionosphere (i.e., no upflowing Alfvénic power).

validation to equation (2).

If we traced the Alfvénic oval from Fig. 16 along magnetic field lines to the outer magnetosphere, we would reach the equatorial region and various boundary regions, likely including the reconnection region, all of which are generator regions of Alfvén waves. In fact, Chaston et al. (2015) provided evidence of enhanced Alfvén wave activity, with frequencies from effectively zero up to 100 Hz in the nightside equatorial plane of the inner edge of the plasma sheet (using Van Allen Probes). The data were collected between October 2012 and March 2015, and were sorted by nonstorm periods, main phase, and recovery phase. Fig. 17 shows the corresponding spatial distributions of wave occurrence. It is noted that since the satellite had an equatorial orbit, as opposed to the polar orbits of FAST and Polar, the format chosen for the spatial distribution was L versus MLT. These distributions indeed resemble the Alfvénic ovals, especially for the nightside (18–06 MLT), from Fig. 16, allowing for some differences in the mapping scheme and the different quantities plotted (i.e., probability of occurrence versus Poynting flux). On the nightside, a clear expansion to smaller L values and a wider longitudinal range of enhanced activity (with values $> 10^{-2}$) is observed during both storm phases (panels b and c), in comparison to the nonstorm phase (panel a). The total power values are not available from this study for comparison with Fig. 16. The dayside also shows increased wave activity during the storm phases, especially the main phase. However, there is generally less wave activity compared to the nightside, in spite of other reports that confirm that the dayside regions also generate significant Alfvénic activity (Johnson et al., 2001; Chaston et al., 2008; Yao et al., 2011). The discrepancy to these other reports might be due to the apogee of the Van Allen Probes being at about 6.5 L, and thus the magnetopause and dayside boundary layers are not regularly crossed, but only during more intense storms.

2.4. Solar wind/IMF dependence

In previous subsections, we have shown that the Alfvénic oval, including its expansion and total power, can be described in a predictable way by the *AE* index, and that the Alfvénic oval is a function of substorm and storm phases. Ultimately, these relationships rely on the uninterrupted but varying flow of energy from the solar wind into geospace. The effects of this coupling on various space regions and processes within them have been intensely studied. For example, Akasofu (1981) lists several functional forms that relate the geomagnetic indices to the various solar wind and IMF parameters. It is now understood that the Alfvénic oval is also predictably impacted by solar wind and IMF parameters, which is the topic of this subsection.

Various coupling functions have been developed to describe the interaction between the solar wind and the magnetosphere (see Newell et al., 2007, for a comprehensive list). Using the coupling function, $\mathrm{d}\Phi_{\mathrm{MP}}/\mathrm{d}t = v^{4/3}B_T^{2/3}\sin^{8/3}(\theta/2)$ (where $\mathrm{d}\Phi_{\mathrm{MP}}/\mathrm{d}t$ is the rate at which magnetic flux is opened at the magnetopause, $B_T = (B_y^2 + B_z^2)^{0.5}$, v is velocity, and θ is the clock angle of the IMF magnetic field), Newell et al. (2009) calculated hemispheric distributions and total power of Alfvénic electrons above the ionosphere during low solar wind driving and moderately high solar wind driving. Similar to studies reviewed above, the peak energy flux lies in the pre-midnight sector (Fig. 18a). Moreover, the total energy flux into the ionosphere increases by a factor of 8.0 (from 0.6 to 4.8 GW) from low to high solar wind driving conditions.

Using the scheme illustrated in Fig. 11, Zhang et al. (2014) investigated the relationship between the upstream solar wind/IMF driving conditions and the simulated hemispheric integrated Alfvénic power using the global MHD model LFM. Fig. 18b combines the results from 18 test runs, while changing the variables in the solar wind coupling function $\varepsilon = vB_T\sin^2(\theta/2)$ (Kan and Lee, 1979). Note that this coupling function is different from that used by Newell et al. (2009). The vertical axis in Fig. 18b is the hemispheric, integrated, 1-h average Alfvénic power flowing into the Northern Hemisphere. Not only does the global Alfvénic power increase with solar wind driving, but the data points exhibit a nearly linear relation, which demonstrates that the Alfvénic power is again predictable based on solar wind/IMF parameters. This is particularly interesting because the *AE* index also shows a linear relationship with Alfvénic power (section 2.1).

To investigate the effect of the IMF orientation on the Alfvénic oval, Hatch et al. (2017) used low-altitude measurements from the FAST satellite. They also compared their results with the IMF-dependence of high-altitude Alfvénic power obtained from the simulation study,

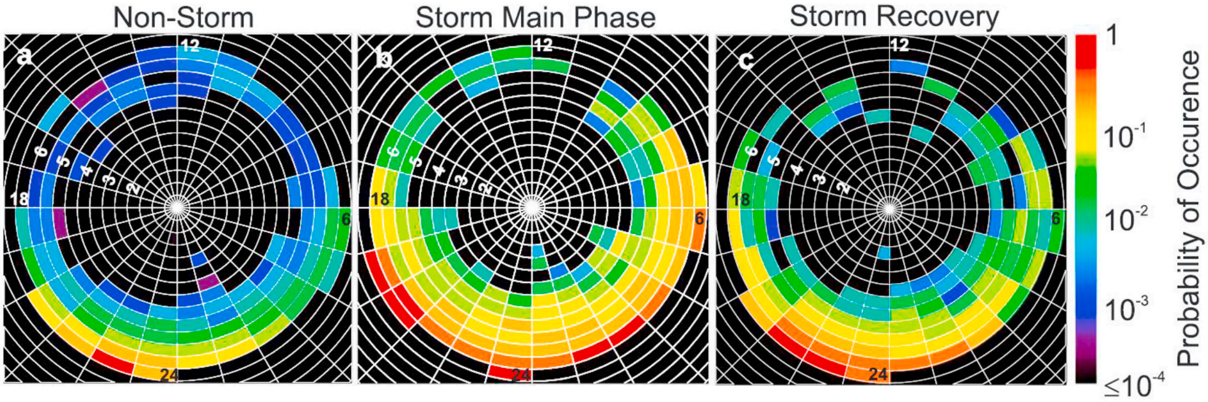

Fig. 17. (From Chaston et al., 2015) Probability of wave occurrence for (a) nonstorm phase ($Dst > -20$ nT), (b) storm main phase, and (c) storm recovery phase. Color scale shows the duration of broadband wave observation in each MLT-L shell bin divided by the time spent in each bin.

already mentioned in the previous paragraph (Zhang et al., 2014). However, while Hatch et al. (2017) used observed values of the solar wind/IMF parameters (within certain constraints; see their study), Zhang et al. (2014) used constant values for driving the simulations throughout the study period. Observed spatial distributions of IAW-associated electron energy flux show a clear dependence on the prevailing IMF orientation (Fig. 19a), with the largest regions of enhanced power occurring under IMF orientations with a southward B_z component (lowest row). Only weak, localized enhancements appear on both the dayside and nightside with a northward B_z component (top row). A dawn-dusk asymmetry effect is also observed for $|B_y| > 0$ (central row).

In comparison, the LFM results show very similar spatial distributions of energy flux, even though they were obtained for a different quantity (Poynting flux), with some notable differences (Fig. 19b). It is noted that this comparison is again an example of the two Alfvénic layers (*cf.* Fig. 5), and as such, morphologically both should be similar. In fact, the similarity is especially apparent for $B_z < 0$ (lower row) and $|B_y| > 0$ (central row). However, while for $B_z > 0$ the observations (panel a) clearly show some Alfvénic activity, the simulations (panel b) show almost no activity. This might be due to the steady driving in the simulations, which does not lead to any wave generation under $B_z > 0$. In contrast, there are always some fluctuations in the actual solar wind/IMF parameters, which generate Alfvén waves that can accelerate electrons. Interestingly, for $B_z < 0$, the magnetosphere does not require any fluctuations in the simulations. This does suggest that the source mechanisms for the Alfvén waves are different for different IMF orientations, as pointed out by Zhang et al. (2014).

In addition to the morphological similarity, it would also be expected that the total integrated, hemispheric wave powers are larger in all cases compared to the corresponding total integrated, hemispheric electron energy fluxes, if we assume that the former drives the latter. However, as already pointed out, for $B_z > 0$, the wave power (panel b) is zero (or close to zero), which cannot explain the corresponding powers of ~0.4 GW for the electron energy flux (panel a). For the other IMF orientations, the total Alfvén wave powers are indeed larger in all cases. It is instructive to apply equation (2), which expresses the absorption efficiency and allows inferring the total power of the secondary oval from that of the primary oval, to these powers. For $|B_y| > 0$, we obtain: 56% of ~2 GW (wave power) equals ~1.1 GW (estimated electron power), which matches reasonably well the observed values of 1.14 to 1.28 GW (electron power). For $B_z < 0$, the situation is quite different: 56% of ~7 GW (wave power) equals ~4 GW (estimated electron power), that is, about twice as large as the recorded electron power (1.89 – 2.13 GW). In this comparison, it should again be noted that the methodologies for the solar wind/IMF inputs differ between observation and simulation studies. While this might explain some of the mismatch, further analysis is required. In particular, it would be desirable to obtain the primary Alfvénic oval under varying IMF orientations above the AAR from measurements (e.g., from Polar) to compare with both the FAST-based distributions and the simulated distributions.

3. Auroral impact

The Alfvénic aurora is associated with discrete auroral features, both at small scale and at mesoscale. Examples are rays (Ivchenko et al., 2005), vortices (Chaston et al., 2010), poleward boundary intensifications (Mella et al., 2011), field line resonances (Liu and Takahashi, 2013) and the poleward border of auroral surges (Mende et al., 2003). All of them together are part of the auroral oval. In section 1.2, we defined this Alfvénic contribution to the visible aurora as the tertiary Alfvénic oval. This implies that an instantaneous, global image of the auroral oval is at the same time an instantaneous, global image of the tertiary Alfvénic oval, although the latter cannot (yet) be separated from the rest of the auroral oval. Global (hemispheric), space-born imaging of the tertiary oval would advance the study of dynamic processes in the magnetosphere, as they are in many cases the sources of the Alfven waves. Some discussion on how to globally image the tertiary Alfvénic oval can be found in Mende (2016), who propose to use optical measurements to infer properties of the precipitating electrons from which one might infer Alfvénic acceleration. While not global, extended ground-based imagery arrays such as THEMIS/GBO (Mende et al., 2008) and the Red-line Emission Geospace Observatory (REGO) (Liang et al., 2016) are beginning to address Alfvénic imaging covering larger regions in the ionosphere. Alternatively, several indirect methods have been used to quantify the global, hemisphere-spanning Alfvénic contributions

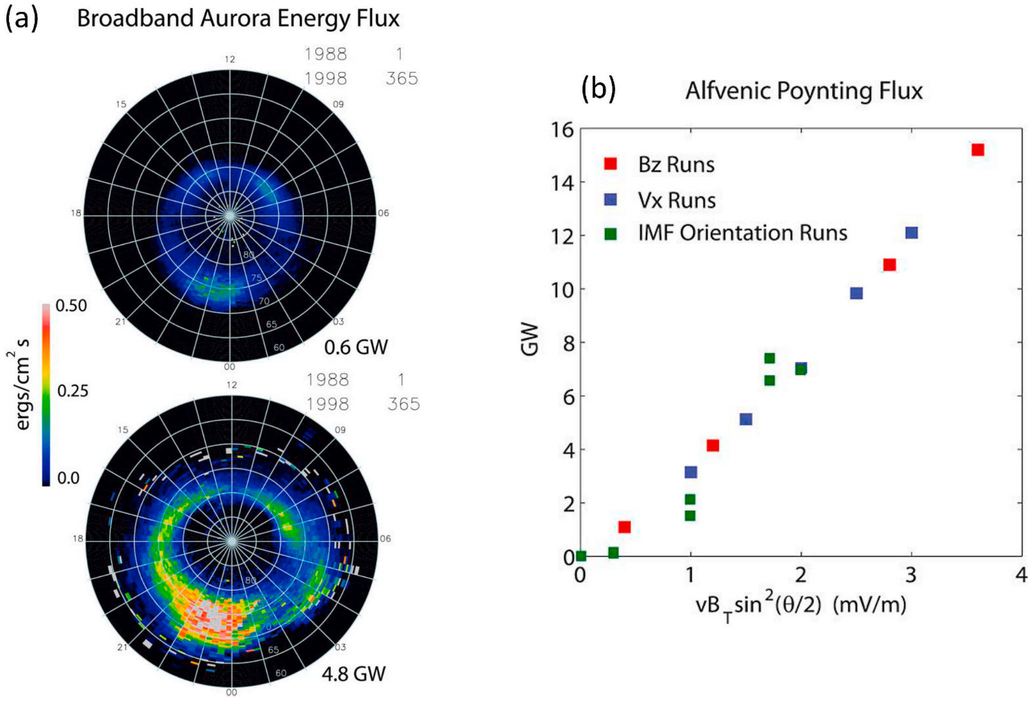

Fig. 18. Solar wind/IMF dependence of the Alfvénic oval. (a) (From Newell et al., 2009) Hemispheric energy flux of Alfvénic electrons for low (one quarter of average strength) and high (50% above average) solar wind driving, using the coupling function $d\Phi_{MP}/dt = v^{4/3}B_T^{2/3}\sin^{8/3}(\theta/2)$. (b) (From Zhang et al., 2014) The relationship between the solar wind coupling function $\varepsilon = vB_T \sin^2(\theta/2)$ (Kan and Lee, 1979) and the hemispheric integrated Alfvénic power derived from 18 test simulations.

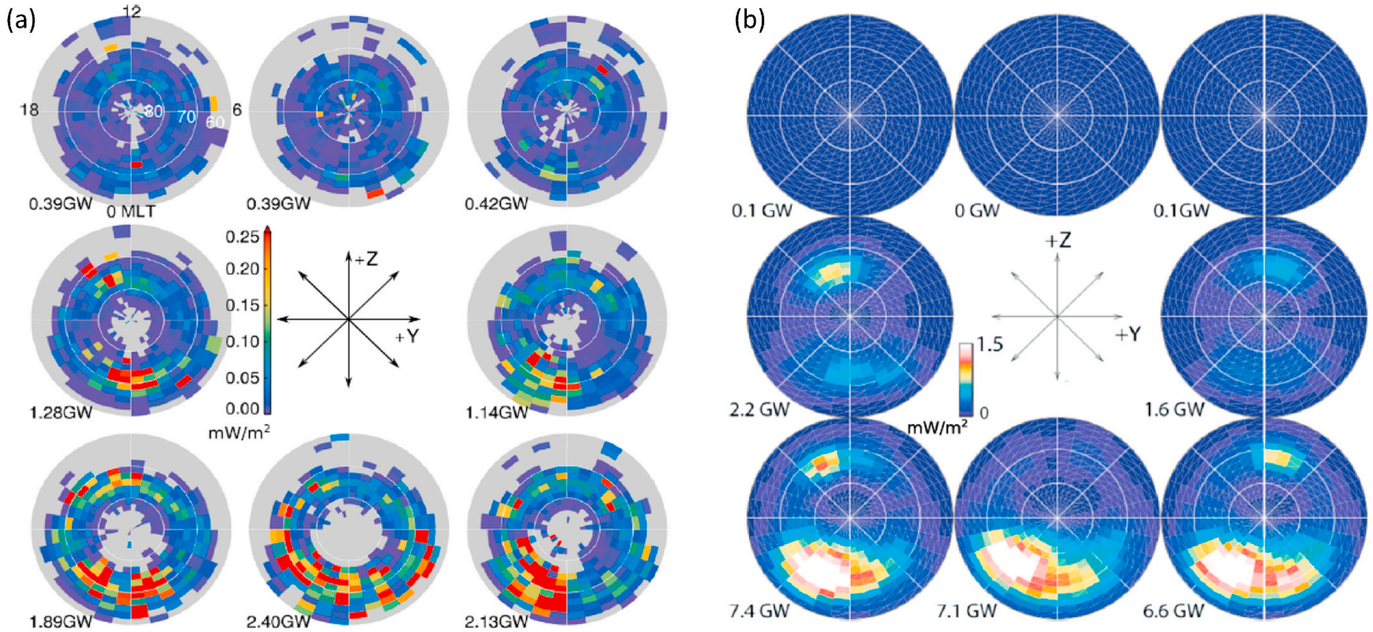

Fig. 19. Comparison of observed secondary Alfvénic oval and simulated primary Alfvénic oval for different IMF orientations. (a) (From Hatch et al., 2017) Distributions of IAW-associated electron energy flux recorded by FAST below the AAR (at < 4000 km). (b) (From Zhang et al., 2014) Simulated 1-h average distributions of downward Alfvénic Poynting flux at 3.5 R_E geocentric distance. Both panels show values mapped to 100 km. The corresponding clock angle of the upstream IMF is indicated in the middle of each panel. The power values (GW) in the lower left corner of each map are the total integrated powers.

to the aurora, the results of which are summarized in Table 2. In the remainder of this section, we provide details about the studies listed in the table.

To identify the Alfvénic part of the aurora, comparisons have been made with statistical global Alfvén wave and electron precipitation maps. Since the *in-situ* data are often averaged over several years in such maps, the auroral images must also be averaged for the comparisons, since the auroral oval shows great variability at any given time. One such comparison is shown in Fig. 20. The image on the left was generated from 17,372 images of the aurora, taken by the UVI camera onboard Polar (Liou et al., 1997). The energy scale was converted to kinetic energy flux due to precipitating electrons (Torr et al., 1995). The high-altitude (4–7 R_E) Alfvénic Poynting flux, shown on the right, was determined from one year (~480 polar orbits) of electric and magnetic field data from the Polar satellite (Keiling et al., 2003). The field-aligned Poynting flux was mapped along converging magnetic field lines to the ionosphere to an altitude of 100 km. It is apparent that both distributions show some similarities. In particular, the most intense region is located at ~2100–0000 MLT for the aurora and the Alfvénic oval. The aurora in this sector is largely associated with auroral substorms (see section 3.2). On the dayside, there is a smaller region (post-noon) of enhanced activity, which partially overlap in both distributions. The noticeably reduced Alfvénic activity on the flank sides would suggest that non-Alfvénic electron acceleration (see section 1.3) dominates on average in these regions. However, the reader is reminded that during geomagnetically disturbed times, the flanks can also show significant Alfvénic activity (e.g., see section 2.3). Since neither of the two distributions was sorted by geomagnetic conditions, less often occurring events do not stand out. From this simple comparison, it was concluded that about one third of the hemispheric aurora could potentially be driven by Alfvén waves (Keiling et al., 2003). However, this is only an upper estimate, because it does not account for the fact that not all Alfvén wave power is absorbed by electrons, as discussed in section 1.3. Applying a global absorption of 56% (see equation (2)), we obtain ~20% for the total auroral electron precipitation driven by Alfvén waves (which is listed in Table 2).

Table 2
Global Alfvénic contributions to the aurora.[a]

Study	Mission/Model	Alfvénic (%)
Keiling et al. (2003) [b]	Polar	20
Chaston et al. (2007) [c]	FAST	25-39, 50
Newell et al. (2009) [d]	DMSP	6–13
Zhang et al. (2015) [e]	LFM	19
Zhang et al. (2015) [f]	OVATION	14
Keiling et al. (2020) [g]	Polar, TIMED	3-10, 18

[a] Direct comparison of values is cautioned due to some differences in regions, conditions and phases utilized by each study.

[b] Average over entire hemisphere; 56% absorption was applied to the reported value by Keiling et al. (2003).

[c] Range for increasing auroral activity averaged over entire hemisphere, followed by pre-midnight region only.

[d] Range from quiet to active solar wind driving for entire hemisphere.

[e] Value is derived for entire hemisphere using values from Zhang et al. (2015) .

[f] Value is derived for entire hemisphere using values from Zhang et al. (2015).

[g] Range from presubstorm to expansion phase for nightside auroral zone, followed by auroral bulge only during expansion.

3.1. *Aurora and geomagnetic activity*

Using the FAST satellite with an orbital range of 300–4400 km, Chaston et al. (2007) conducted a 2.3-year statistical study combining measurements of fields and particles. Fig. 21a shows the statistical distribution of the total electron energy deposition, which is highest in the midnight sector. The fraction of this power that was provided by electron fluxes with distributions consistent with the acceleration by Alfvén waves, and simultaneously occurring Alfvén waves, is shown in Fig. 21b. Near pre-midnight, this fraction is ~50% on average, while it is 31% over the entire high-latitude region. Furthermore, the authors differentiated the Alfvén wave contribution according to auroral activity and found that the power fraction increases from 25% to 39% for the entire hemisphere as the activity increases (Fig. 21c). These Alfvénic contributions are listed in Table 2. It was concluded that, in the vicinity of the pre-midnight auroral oval, Alfvén waves may provide the dominant

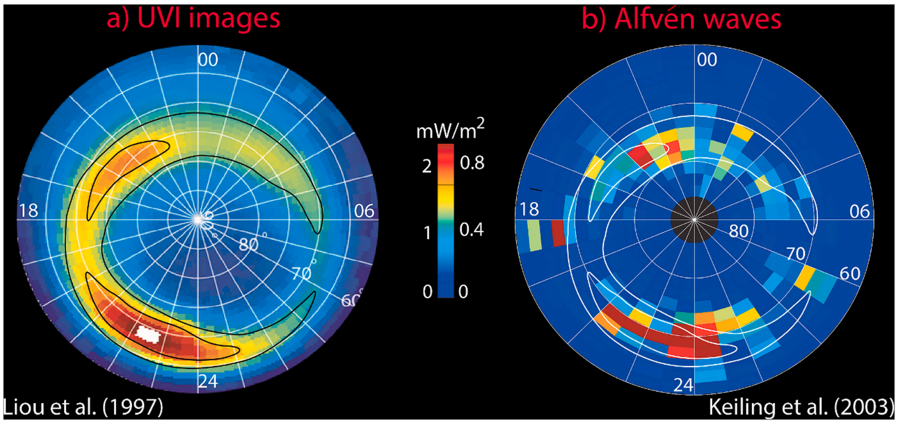

Fig. 20. Comparison of the average auroral luminosity and the average, primary Alfvénic oval (from Keiling et al., 2003). Approximate contour lines (drawn by hand in panel a and copied into panel b) were added to the original figures as a visual aid. (a) Average auroral intensity in the Northern Hemisphere recorded in the UV spectrum [Lyman-Birge-Hopfield (long)]. The figure is composed of 17,372 images taken by the UVI instrument on board Polar during four months of operation. (b) Average wave Poynting flux flowing into the AAR in the Northern Hemisphere, as measured at high altitudes (4–7 R_E geocentric distance) over one year and scaled along converging magnetic field lines to ionospheric altitude (100 km). This figure is the same as Fig. 4b.

contribution for powering electron acceleration during active times. The study also showed that while there is still Alfvén wave activity at FAST altitudes, its associated power is only about 10% of the concurrent kinetic energy flux of the electrons, and therefore, additional Alfvénic electron acceleration below FAST would not significantly change the statistical results of this study.

A similar approach was taken by Newell et al. (2009), although they did not test for the presence of Alfvén waves as Chaston et al. (2007) had done. The electrons were sorted by monoenergetic and broadband (Alfvénic) acceleration characteristics, and the remaining electrons were declared to cause diffuse aurora. From this, proportions were calculated to estimate the contribution of each type to the aurora. Overall (i.e., entire hemisphere), it was reported that the Alfvénic aurora contributes 6% during quiet periods and 13% during active periods (the corresponding data are shown in Fig. 18a). These values are also listed in Table 2. It was also reported that the Alfvénic aurora exhibits the most rapid relative increase with rising activity, increasing by a factor of 8 from low to high driving. Recently, Dombeck et al. (2018) challenged these results, arguing that the contribution of the diffuse aurora was significantly overestimated, which would in turn affect the proportion of the Alfvénic aurora as well. The interested reader is referred to this study for further details.

It was mentioned above that the “instantaneous” tertiary (visible) Alfvénic oval cannot be separated from the other parts of the visible auroral oval (in a global sense). However, by using mathematical relationships for the dependences of the global Alfvénic power and the global Alfvénic electron energy flux on geomagnetic indices, we can indirectly determine the “instantaneous” global proportion of the tertiary oval. Here is an example, applied to some data from Meng and Liou (2002). Fig. 22a shows a sequence of nightside auroral images during an auroral substorm, using UVI images from Polar. During the half-hour time interval, the aurora undergoes significant changes. The lower panels show the *AE* index and the inferred global auroral power, spanning an extended time interval (6 h) which includes both the expansion and the recovery phases. The correlation of both quantities is very noticeable. The associated aurora occurs largely on the nightside, allowing us to use two relationships, which were derived for the nightside auroral zone, for the integrated power of the primary and secondary Alfvénic ovals with respect to the *AE* index:

Newell and Gjerloev (2011):

$$FE\ [\mathrm{GW}] = 0.005\ \mathrm{GW/nT} \cdot AE\ [\mathrm{nT}] + 0.1\ \mathrm{GW} \tag{5}$$

Keiling et al. (2019b):

$$AW_{inflow}\ [\mathrm{GW}] = 0.009\ \mathrm{GW/nT} \cdot AE\ [\mathrm{nT}] + 0.07\ \mathrm{GW} \tag{6}$$

(Note: While equation (5) is the same as equation (3) and reproduced here for convenience, equation (6) is different from equation (4). In equation (6), the total inflowing power is used, whereas in equation (4), the net inflowing power was used.)

Fig. 22b shows all power values, observed and calculated, in direct comparison. The power ratio of the auroral power, which contains all types of aurora, and the secondary Alfvénic oval (i.e., Alfvénic electron precipitation), obtained from equation (5) with *AE* applied, yields the overall Alfvénic contribution. This example yields a contribution of 6–13%, varying throughout the substorm cycle (note the different scale for auroral and electron power in panel b). The global inflowing power of the primary Alfvénic oval, obtained from equation (6) with *AE* applied, is also shown for comparison. Alternatively, applying the 56%-absorption coefficient [see equation (2)] to this primary Alfvénic oval would also yield the global power of the secondary Alfvénic oval, which

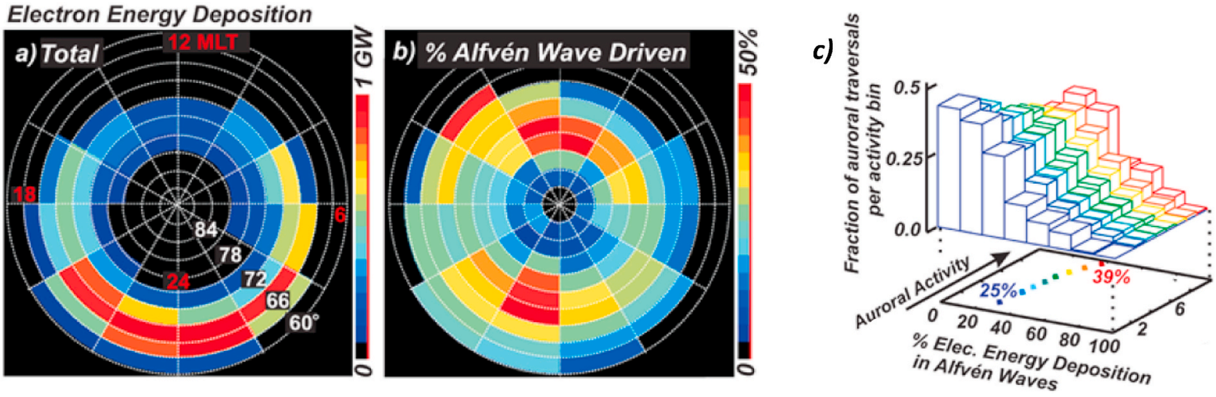

Fig. 21. (From Chaston et al., 2007) Statistical distributions using FAST data in the altitude range from 300 to 4400 km. (a) Average total electron energy deposition. (b) Percentage of the total electron energy flux associated with Alfvénic acceleration.

(a) Auroral development during auroral substorm

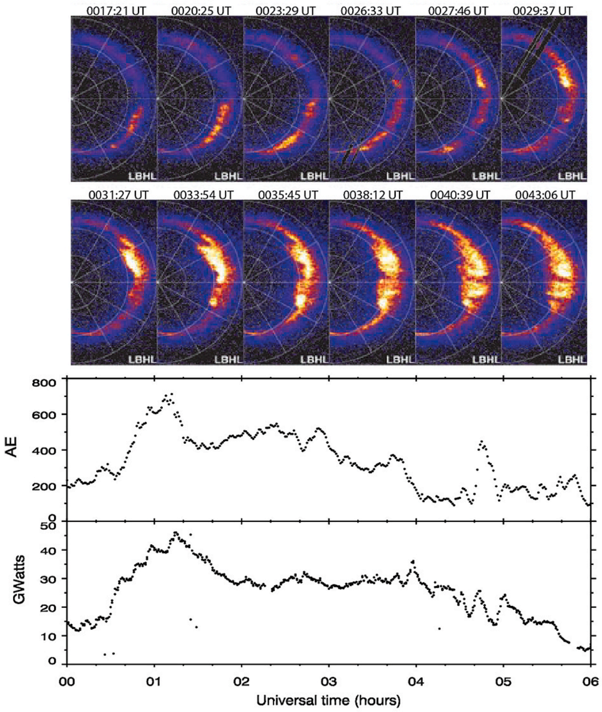

(b) Comparison of auroral oval with primary and secondary AO

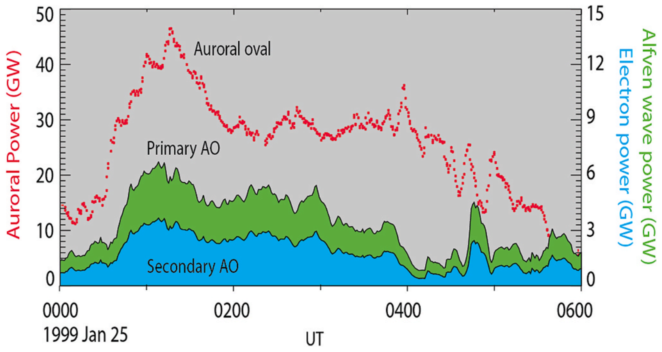

Fig. 22. Illustration of the usage of the *AE* index to calculate the Alfvénic contribution to the aurora. (a) (From Meng and Liou, 2002) Auroral images and the associated auroral power and *AE*. (b) Comparison of auroral power with primary and secondary Alfvénic ovals (AO), using the *AE* index for calculation. The auroral power is redrawn from the last panel of (a).

is here shown by directly applying equation (5) instead.

Alternatively, one can also infer the global Alfvénic contribution to the aurora by comparing statistical estimates of total electron precipitation (e.g., Akasofu, 1981; Østgaard et al., 2002) with those for Alfvénic electrons (Newell and Gjerloev, 2011). For example, using Akasofu's equation (U_A [GW] $= 0.05$ GW/nT $\cdot$ *AE* [nT]) and Newell and Gjerloev's equation (*FE* [GW] $= 0.005$ GW/nT $\cdot$ *AE* [nT], ignoring the intercept), the global contributions of Alfvén wave power to the aurora would be a constant 10% ($= 0.005/0.05$).

3.2. Substorm aurora

In the previous section, an expanding auroral oval during a substorm was shown with several near-instantaneous space images (Fig. 22). A different format is given by Liou et al. (2013), who averaged 2.5 years of auroral images to generate average distributions of the aurora of isolated substorms with respect to the three substorm phases (Fig. 23a). Growth, expansion and recovery can clearly be identified, with the expansion covering the pre-midnight region between 20 and 1 MLT. Such averaged auroras are suitable for comparison with statistical, *in-situ* data of the Alfvénic oval. Panels (b) and (c) show corresponding averaged distributions of Alfvénic power (primary Alfvénic oval) and Alfvénic electron energy flux (secondary Alfvénic oval), respectively, sorted by substorm phase. The distributions for each substorm phase are remarkably similar, especially with regard to the auroral bulge region of the expansion (see added approximate contour lines outlining the average auroral bulge). This similarity supports the causal relationship, as illustrated in the layered scenario of Fig. 5. It should be emphasized that panel (a) shows all types of auroras (that is, the Alfvénic aurora is only one part of it). From a comparison of the intensities in each panel, the following can be tentatively inferred. There appears to be enough power in the primary Alfvénic oval (panel b) to drive the secondary Alfvénic oval (panel c). However, the auroral power (panel a) is significantly larger than those of the other two, which can be attributed to the fact that the aurora does not only comprise the Alfvénic aurora (i.e., tertiary Alfvénic oval) but also the other auroral types. In the following, we review studies that in more detail extracted information about the Alfvénic contribution to the aurora during each of the three substorm phases.

Fig. 24 is a collection of different studies for the estimation of the Alfvénic contributions to the substorm aurora. While the left side considers the entire nightside auroral oval (18–06 MLT), the right side focuses on the pre-midnight region (21–24 MLT), which statistically coincides with the substorm auroral bulge. Both sides follow the same structure. The top panel shows the integrated auroral power as a function of time in relation to substorm onset. The auroral data were obtained from ultraviolet imagers on board the TIMED satellite (Liou et al., 2013) and the Polar satellite (Newell et al., 2001), respectively. Three distinct regions, which correspond to the three substorm phases, can be identified: growth, expansion, and recovery. These data have been compared with the statistical data obtained from high-altitude satellite measurements of Alfvénic Poynting flux as a function of substorm phases, as shown in the middle panel (Keiling et al., 2020). In the middle panel, the auroral data (regression lines only) are reproduced (red dashed lines) from the top panel for comparison with the Alfvénic power above the AAR (blue lines). The blue shaded region spans the range from the lower to upper limits of wave deposition below Polar. It is clear that the Alfvén wave power is not the major contributor overall in either case, that is, the entire nightside auroral zone and the auroral bulge. This can also be seen in the panel below, showing the percentage of total inflowing Alfvén wave power (blue line) and the resulting 56% electron absorption (green dotted line) (*cf.* equation (2) of section 1.3). For the nightside auroral zone, the total Alfvén wave power is about 5% of the total amount of auroral power during the early growth phase and the late recovery phase, while growing to 17% during the expansion phase. Allowing for the estimated global absorption efficiency of 56%, about 3% (growth) and 10% (expansion) of the aurora are potentially driven by Alfvén waves. For the statistical location of the auroral bulge, the Alfvénic contributions are larger percentagewise, owing to the fact that Alfvén waves are especially generated in this region during substorms. Total inflowing Alfvénic power reaches as high as 32% during the expansion phase (compared to the total auroral power), and about 13% and 7% during the early growth and late recovery phases, respectively. Again, allowing for the global absorption efficiency, actual Alfvénic power contributions reduce to about 18% (expansion), 7% (growth), and 4% (recovery) of the total auroral power.

At the bottom of each side of Fig. 24, the same results are graphically illustrated in the form of a Venn diagram. First, the Alfvénic aurora (i.e., Alfvénic electrons in the diagram) comprises a larger share of the aurora during the expansion phase compared to the growth phase. Second, this increased share is proportionally larger for the auroral bulge compared to the entire nightside auroral zone.

3.3. *Storm aurora*

The most intense and widespread auroral display occurs during geomagnetic storms (*cf.* Fig. 1). The statistical auroral oval grows from a thin oval at higher latitude to a widened oval extending to lower latitudes with increasing geomagnetic activity, as shown in Fig. 25a. In section 2.3, it was shown that the Alfvénic oval (primary and secondary) undergoes very similar changes. For example, in Fig. 16a, the nonstorm and storm (primary) Alfvénic ovals compare well with the location of the averaged aurora for quiet periods (Q = 0) and the most active times (Q = 7), respectively (e.g., compare latitudinal changes for different MLTs).

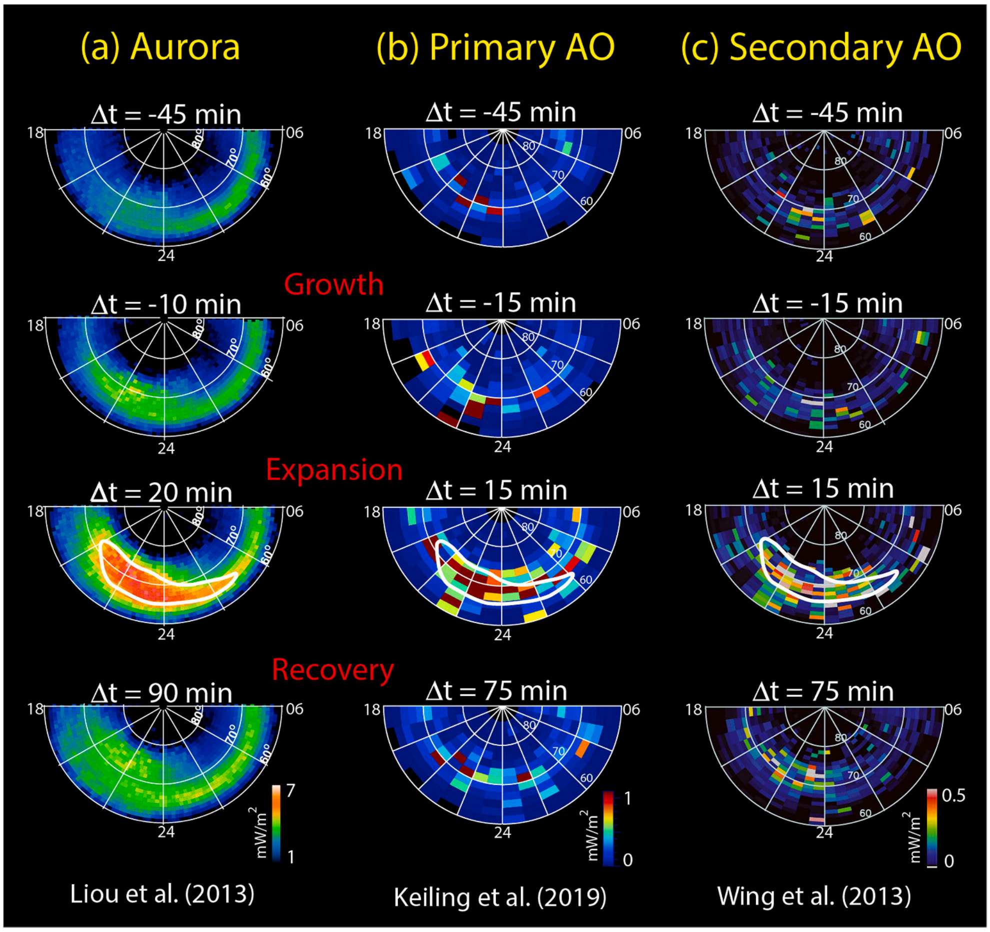

Fig. 23. (Modified from Keiling et al., 2020) Temporal evolution of power during a substorm cycle ($\Delta t = 0$ corresponds to the onset time) obtained by different statistical studies. (a) Auroral power measured by the ultraviolet imager of the TIMED satellite (5.5-year database). (b) Alfvén wave Poynting flux measured by Polar (6-year database) between 4 and 7 R_E. Each panel covers 30 min centered at the time labeled. AO stands for Alfvénic oval. (c) Alfvénic electron energy flux measured by DMSP (multi-year database) at 845 km altitude. Each panel covers 15 min centered at the time labeled.

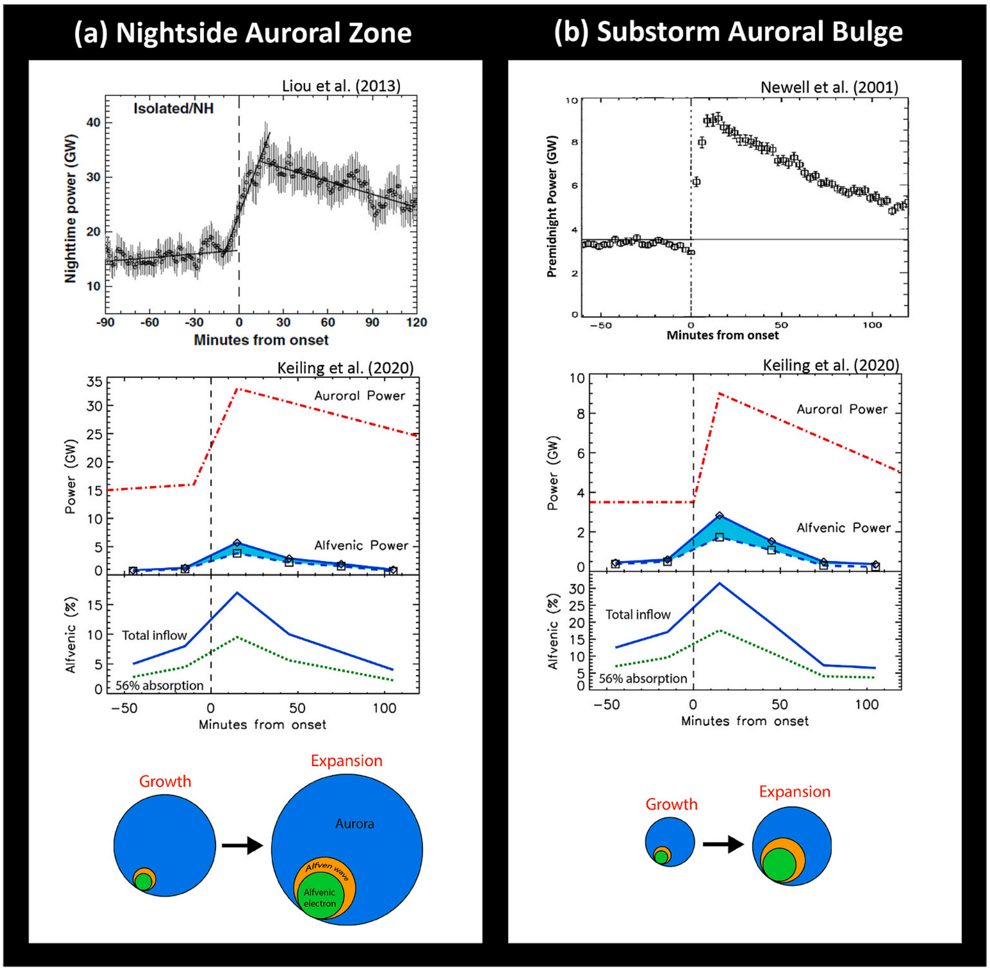

Fig. 24. Statistical estimates of Alfvénic contributions to the aurora during substorms for (a) the nightside auroral zone and (b) the auroral bulge. Both panels are equally structured. (Top) Superposed epoch analysis of auroral power. The vertical dashed line marks the substorm onset. (Middle) Comparison of Alfvén wave power above the AAR and auroral power (red) in relation to substorm phases for the nightside auroral zone. The blue solid and dashed lines show the total power and net power, respectively, entering the AAR from the magnetotail. The auroral power curve is the linear trend of the auroral data from the top panel. The dashed vertical line marks the substorm onset. The lower panel shows the Alfvénic contribution (in percent) in relation to substorm phases. The green dotted line is the 56%-absorption line. (Bottom) Venn diagrams to illustrate the proportional contributions of global Alfvén wave power and Alfvénic electron power in comparison to the auroral power.

An alternative format of Fig. 16a is shown in Fig. 25b, where only the peak values of Alfvénic Poynting flux during storm times for the entire period under investigation are shown for each grid cell (Keiling et al., 2019a). While this is not to be interpreted as an instantaneous image of the primary Alfvénic oval, it gives a sense of where very intense Alfvénic aurora can occur throughout a storm. The dashed lines outline the aurora at Q = 7 from panel (a), which overlaps with much of the very intense regions of Alfvénic Poynting flux. While this suggests that some of the energetic Alfvén waves would certainly contribute to the storm aurora, it would again not account for the entire aurora. From panel (b), one can also infer that many regions (grid cells) experience Alfvénic Poynting fluxes of 100 mW/m^2, and up to 500 mW/m^2 (mapped to the ionosphere), which are some of the largest values recorded in the magnetosphere.

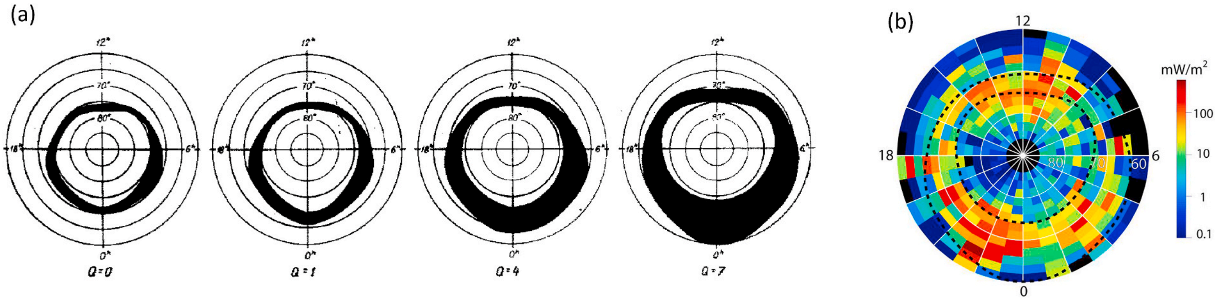

Fig. 25. Comparison of the auroral oval and Alfvénic oval for different activity levels. (a) (From Feldstein and Starkov, 1967) The auroral oval at different degrees of geomagnetic activity. (b) (From Keiling et al. (2019a) The global distribution of peak wave Poynting flux during storms ($Dst < -40$ nT) flowing toward Earth as measured at high altitude (4–7 R_E geocentric) in the Northern Hemisphere obtained from 6 years of Polar measurements and scaled along converging magnetic field lines to ionospheric altitudes (100 km). The two dashed oval-shaped curves delineate the statistical auroral oval for geomagnetically active periods (Q = 7) of panel (a).

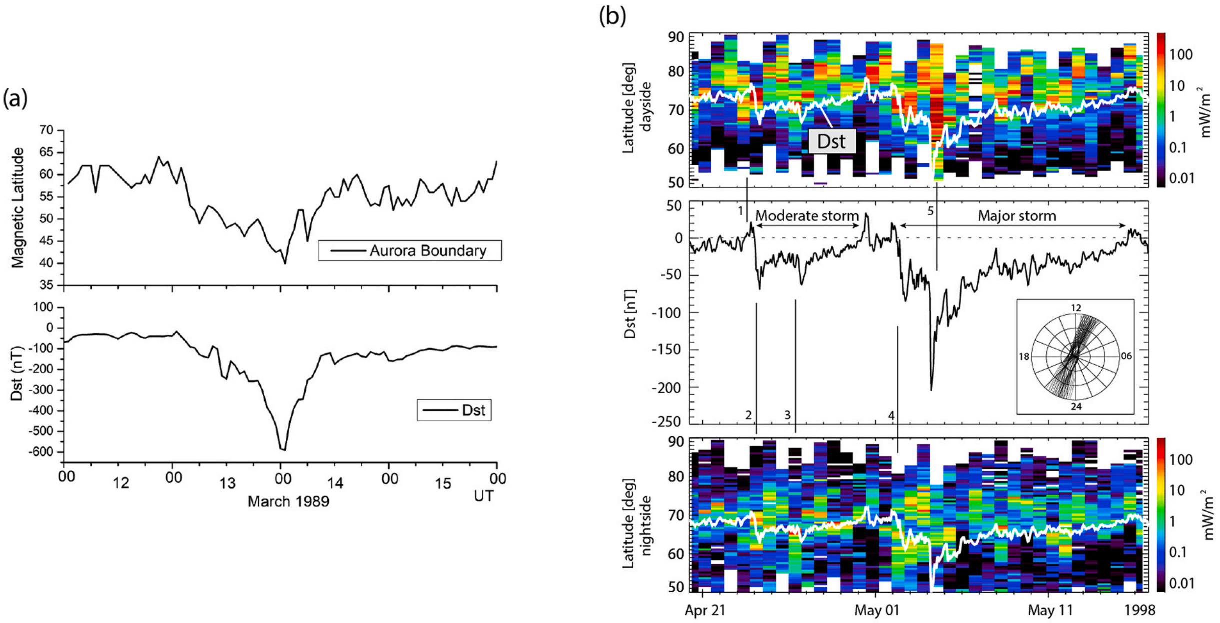

Fig. 26. The Alfvénic aurora during geomagnetic storms. (a) (Slightly modified from Boteler, 2019) *Dst* and auroral boundary during the March 1989 storm. (b) (From Keiling et al., 2019a) Tracing Poynting flux along Polar's orbit during a period of 27 days, which includes a moderate storm and a major storm. (Top) Peak values of Poynting flux binned by 0.5° magnetic latitude (y axis) versus days (x axis) and mapped using the T01 model. Each column represents the section of a Polar orbit within 50° and 90° magnetic latitude. Only values obtained when Polar was on the dayside are included. The *Dst* curve (middle panel) is overlaid (white line) with an arbitrary scale for illustrative purposes. (Middle) *Dst* index versus time, with labels indicating a moderate and a major storm. Numbered vertical lines (1–5) refer to the features in the panels above and below. The inset shows Polar's daily orbits during the time period shown here projected onto the latitude-local time plane. (Bottom) The same data quantity as in the top panel but for the nightside with the *Dst* curve overlaid.

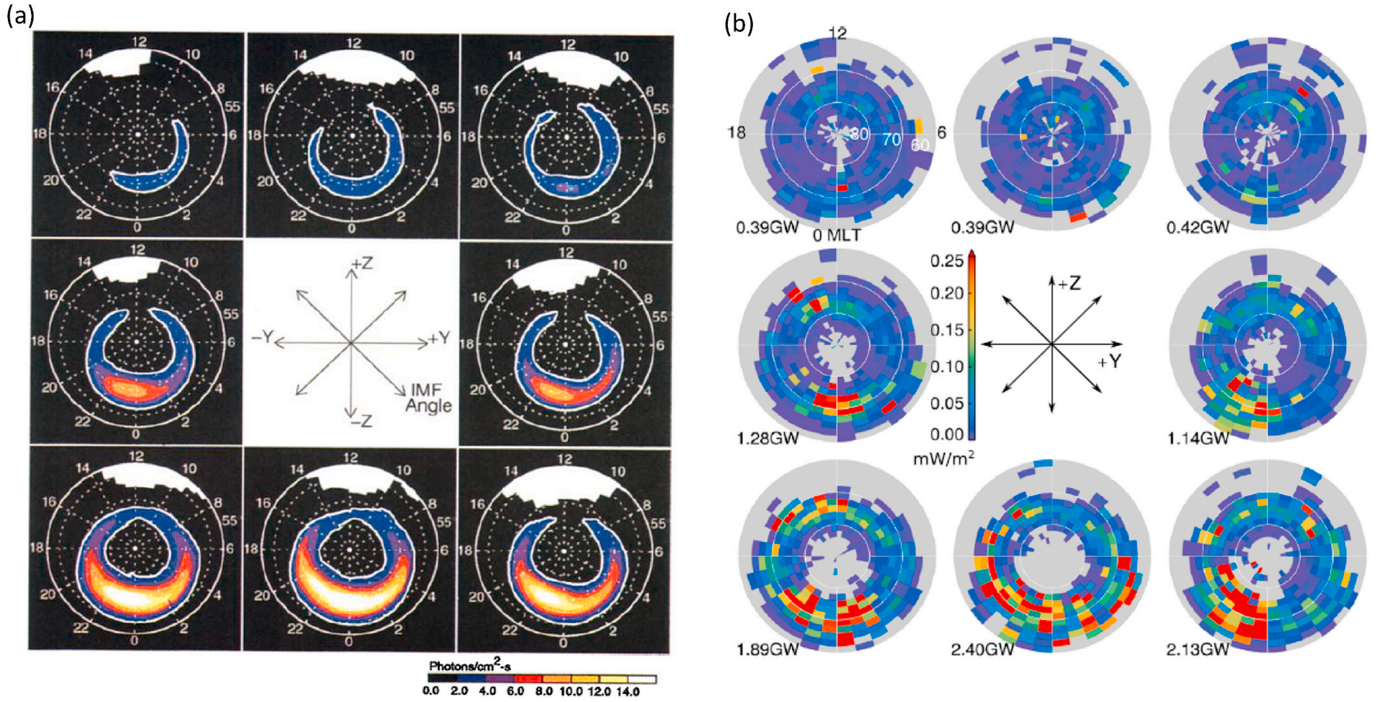

Fig. 27. Comparison of auroral oval and observed secondary Alfvénic oval for different IMF orientations. (a) (From Shue et al., 2001) Mean auroral pattern in winter, using the LBHL filter of the UVI instrument onboard Polar. A contour of 2 photons $\mathrm{cm}^{-2}\ \mathrm{s}^{-1}$ is marked as an area of bright aurora. (b) (From Hatch et al., 2017) Distributions of IAW-associated electron energy flux recorded by FAST below the AAR. (Same as Fig. 19a).

Instead of using an average format, Fig. 26a shows the expansion of the auroral border with the *Dst* index for a period of four days. The variation in the auroral boundary follows the variation in the *Dst* index. We emphasize that all auroras are included in this comparison. To get a sense for the Alfvénic aurora, Fig. 26b shows a period of 27 days, correlating the expansion of the Alfvénic oval (in particular, its lower boundary) with the *Dst* index. Each vertical strip shows the Poynting flux along one Polar satellite orbit. The white line shows the *Dst* index (same as the middle panel of Fig. 26b). Hence, it can also be concluded that the variations of the Alfvénic oval follow the variation in the *Dst* index, and by inference, the Alfvénic oval follows (in shape) the auroral boundary. It was noted by Keiling et al. (2019a) that the agreement is better for the dayside. The nightside contains additional Alfvénic oval variations that can be attributed to substorm activity in the magnetotail (Keiling et al., 2020). While this is only indirect evidence (i.e., comparing the borders of the auroral and Alfvénic ovals), it is nonetheless suggestive that the Alfvén waves contribute to the expansion of the auroral oval during storms. The reader is referred back to Table 1 (section 2.3) for estimates of global, hemispheric powers of the primary and secondary Alfvénic ovals during storms. The estimate of the latter is also an estimate of the tertiary Alfvénic oval, assuming that all Alfvénic electrons cause aurora.

3.4. Solar wind/IMF-controlled aurora

While it has long been known that the global auroral distribution responds to solar wind/IMF changes, it was reviewed in section 2.4 that the primary and secondary Alfvénic ovals also show clear spatial patterns, in particular, related to the orientation of the IMF. It is instructive to compare the resulting patterns of the auroral oval and Alfvénic oval to test if it supports a causal relationship as well. This comparison also provides a method of estimating the overall percentage of Alfvénic contributions to the solar wind/IMF-driven aurora (see below).

Shue et al. (2001) generated average, global auroral patterns using $\sim$1 year of images from the Polar UVI imager sorted by the IMF orientation and by season (Fig. 27a). In comparison, Fig. 27b shows the spatial distributions of IAW-associated electron energy flux recorded by FAST below the AAR (Hatch et al., 2017). There is good agreement between the corresponding maps in terms of where the more intense regions are located inside the oval. The activity is high on the nightside (with some asymmetry) for southward IMF, and reduces as the IMF rotates from a southward to a northward direction. For $|B_y| > 0$, both studies report smaller but well-defined regions of enhanced activity on the nightside. Under northward IMF, the dayside aurora shows very little to no activity, while the Alfvénic oval still shows some enhancement, albeit also significantly reduced. It is noted that panel (a) shows the winter season only. The summer distribution (not shown here) shows more auroral activity during northward IMF, especially pre-noon, and thus more closely resembles the distribution of Fig. 27b. The reader is referred to Shue et al. (2001) for more detail on the seasonal effects of the auroral oval. Hatch et al. (2017), on the other hand, averaged over all seasons, and thus, their results contain all features that might be season dependent, potentially explaining some of the differences between panels (a) and (b). Again, we emphasize that the auroral images contain all types of aurora, and thus a perfect match to the Alfvénic oval would not be expected anyway.

Numerical simulations have also generated the Alfvénic oval in response to solar wind driving as already reviewed in section 2.4. Here we review the study by Zhang et al. (2015) who performed a data-model comparison (Fig. 28) for an actual event using global MHD simulations coupled with an electron precipitation model, and the OVATION Prime model from Newell et al. (2014). Six hours of solar wind/IMF data were utilized as input for both models. Fig. 28a shows that the hemispheric broadband electron power (red dots) predicted by OVATION Prime increases approximately linearly with the coupling function $d\Phi_{MP}/dt = v^{4/3}\,(B_y^2 + B_z^2)^{1/3}\,\sin^{8/3}(\theta)$ (Newell et al., 2007), using the same nomenclature as above. The simulated hemispheric broadband power (green crosses) also increases but with a relatively large scatter. Using moderate driving conditions ($d\Phi_{MP}/dt = 1$ MWb/s), Fig. 28b and c shows the hemispheric distributions of broadband electron precipitation for both models (LFM and OVATION Prime). Both distributions exhibit a dawn-dusk asymmetry. The main enhancement in the intensity occurs on the nightside in the pre-midnight sector of 2100–2400 MLT with similar energy fluxes. However, the simulated pattern is located approximately 4° MLAT higher than the empirical pattern. Additional intensity enhancements are seen in both distributions on the dayside. This time, the magnitudes differ significantly from each other. Overall, the total power values are comparable: 4.86 GW and 4.07 GW (upper left corner of each distribution).

Zhang et al. (2015) conducted similar comparisons for mono-energetic and diffuse electron precipitation. While we do not review them here, we make use of the reported total integrated powers to estimate the Alfvénic contribution to the aurora as would follow from LFM and OVATION Prime. From Fig. 28b and c, as already mentioned, we obtain 4.86 GW and 4.07 GW, respectively. Similarly, from Zhang et al.

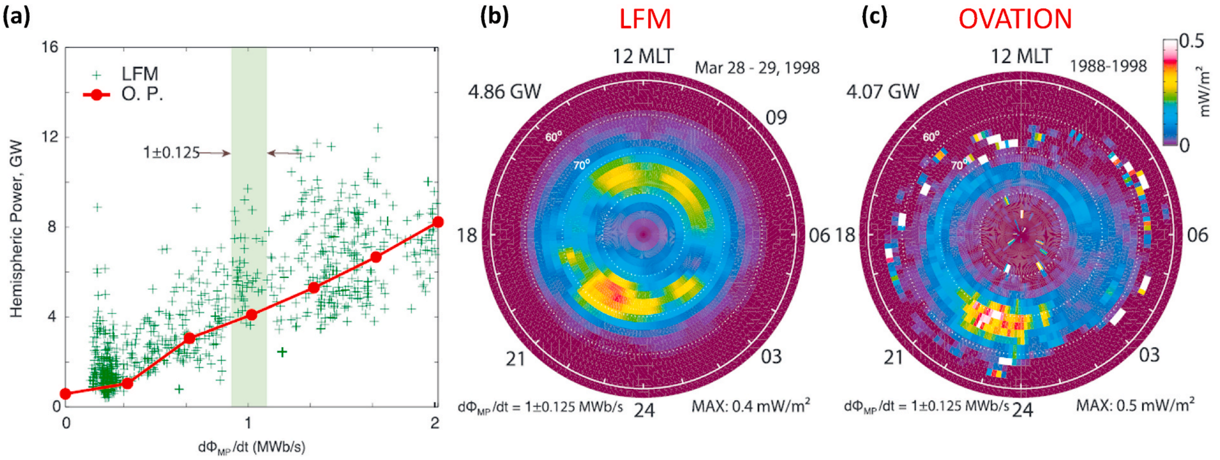

Fig. 28. (From Zhang et al., 2015) Solar wind/IMF-controlled aurora. (a) The relationship between the hemispheric broadband electron power and the effective solar wind coupling function $d\Phi_{MP}/dt$ (green crosses from LFM simulations), superposed with the corresponding OVATION Prime prediction (red dots and red line); (b) the average distribution of broadband electron precipitation corresponding to $d\Phi_{MP}/dt = 1$ MWb/s, derived from LFM; and (c) the distribution of broadband electron precipitation corresponding to $d\Phi_{MP}/dt = 1$ MWb/s, predicted by OVATION Prime.

(2015), we obtain total integrated power values of 21.3 GW (LFM) and 24.1 GW (OVATION Prime), respectively, by combining the monoenergetic and diffuse precipitation powers. Adding the Alfvénic contributions to these values, we obtain the total auroral power of 26.16 GW (4.86 GW + 21.3 GW) and 28.17 GW (4.07 GW + 24.1 GW), respectively. Then, we can calculate the Alfvénic contribution to the entire auroral oval as ~19% (4.86/26.16) and ~14% (4.07/28.17), as inferred from the LFM and OVATION Prime models, respectively. These values are again listed in Table 2 for comparison with the other statistical values.

4. Summary and conclusions

The Alfvénic oval waxes and wanes under changing geomagnetic conditions and solar wind/IMF conditions, as the auroral oval does but not in an identical manner. Similar to auroral forecasting, we ultimately want to be able to predict the morphology, dynamics and total power of the Alfvénic oval (ideally, for all three layers), a challenge that has seen advances in the last two decades. Such predictive power would not only be useful for future events, but also allow us to reinvestigate past events. In this review, we combined the results from multiyear observational studies (utilizing different satellites in different regions), global simulations and empirical models. We find the results to be consistent, which leads to a unified understanding of the M-I coupling of the Alfvénic oval. In this coupling, the AAR has profound effects on the Alfvénic oval as its components, be it Alfvén waves or Alfvénic electrons, propagate toward the ionosphere, where some of the energy is displayed in the Alfvénic aurora. This transformation led us to broaden the definition of the Alfvénic oval to include the primary, secondary, and tertiary Alfvénic ovals.

Overall, this review demonstrates that the Alfvénic oval is sufficiently well-defined and investigated to give it its name. Statistically, there is an oval-shaped distribution of enhanced Alfvénic activity in space, comprised of both Alfvén waves and Alfvénic electrons. While the Alfvénic oval must also exist instantaneously, it is impossible to probe it instantaneously in its entirety in space. The best candidate for capturing the Alfvénic oval is the visible layer, i.e., the tertiary Alfvénic oval. While ground-based imagery has contributed in this endeavor, technological advances in spacecraft instrumentation and/or data interpretation are needed. Such global, space-born imaging of the tertiary oval would likely advance the study of dynamic processes in the magnetosphere, as has global, space-born imaging of the visible auroral oval.

The state of the magnetosphere has been described with geomagnetic indices, such as *AE* and *Dst*, and also in terms of substorm and storm phases. Similarly, the direct control of the solar wind/IMF on magnetospheric parameters is well known. The Alfvénic oval, with its global distribution and global power, is a more recent concept that has been shown to also follow statistical patterns as functions of *AE*, *Dst*, substorm and storm phases, and solar wind/IMF. In light of this review, we conclude that the statistical Alfvénic oval is predictable, within a reasonable range, given geomagnetic conditions or solar wind/IMF parameters. Its dynamic behavior can be summarized as follows:

4.1. *AE index*

1) With increasing *AE*, the spatial extent of the enhanced Alfvénic power grows in longitude and latitude inside the Alfvénic oval.
2) The Alfvénic oval's total hemispherical powers (both Alfvén waves above the AAR and Alfvénic electrons below the AAR) grow linearly with the *AE* index, of which the latter has a shallower slope.
3) For all investigated *AE* values, the Alfvén wave power inflow (from the magnetotail into the AAR) is significantly larger than the power outflow (out of the AAR toward the magnetotail); the estimated net wave power flowing into the AAR is sufficient to account for the integrated precipitating Alfvénic electron power in the nightside auroral zone below the AAR.
4) The global Alfvén wave absorption (by electrons) inside the AAR is 56%. About 33% (upper limit) of Alfvén waves entering the AAR (from above) are reflected, either within the AAR or the ionosphere. An excess wave power of 11% (lower limit) is available for other energy conversion processes.
5) In summary, the oval's size and integrated power strongly depend on the magnetic disturbance level.

4.2. *Substorm*

1) The Alfvénic oval's expansion and total auroral zone power vary with the substorm phases. The oval's growth is sudden and intense at substorm onset. The Alfvénic oval develops a "bulge" at the same location (statistically) as the auroral substorm bulge.
2) The peak inflowing global wave power during the expansion phase is 5.7 GW during unconditioned substorms (i.e., averaged over all types of substorms), 5.6 GW during nonstorm-time substorms, and 7.8 GW during storm-time substorms. These numbers correspond to power increases with respect to pre-onset values of 138%, 366%, and 200%, respectively. (These values were not reviewed here and can be found in Keiling et al., 2020.)
3) The peak precipitating Alfvénic electron power during the expansion phase is 3.4 GW during unconditioned substorms, 2.3 GW during isolated substorms, and 4.3 GW during recurrent substorms. These numbers correspond to power increases with respect to pre-onset values of 84%, 186%, and 64%, respectively. (These values were not reviewed here and can be found in Newell and Gjerloev, 2011.)
4) The Alfvénic aurora is most dynamic (in terms of power changes) during substorms in comparison to other auroral types.

4.3. *Storm*

1) The Alfvénic oval differs significantly for nonstorm periods and storm periods. The oval width and power vary with the storm phases, being the largest and most intense during the main phase. During the main phase, its maximal extent covers latitudes between 50° and 85°.
2) Alfvénic oval growth is fourfold for Alfvén waves (from 2.59 to 10.05 GW) above the AAR, and fivefold for Alfvénic electrons (from 0.54 to 2.62 GW) below the AAR, from nonstorm to storm periods (Table 1).
3) During storms, the Poynting flux associated with individual Alfvén waves can reach values of up to about 0.5 W/m^2 (mapped to ionospheric altitude).

4.4. *Solar wind and IMF*

1) The Alfvénic oval's power grows linearly with the intensity of the solar wind driving.
2) Its relative growth in power is the largest compared to other auroras, increasing by a factor of 8.0 from low to high solar wind driving.
3) The IMF orientation has significant and predictable effects on the spatial patterns of the Alfvénic oval, which resemble those of the auroral oval during similar IMF conditions.
4) The hemispheric Alfvénic power is largest under southward IMF orientations, with wave power intensified on both dayside and nightside. Only weak localized enhancements appear on both the dayside and nightside for northward IMF orientation.

4.5. *Aurora*

1) The contribution of the Alfvénic aurora to the aurora is activity dependent.
2) 10–30% of the aurora is driven by Alfvén waves during active times.
3) 18–50% of the optical intensity in the auroral bulge (pre-midnight region) is driven by Alfvén waves.

4) The Alfvénic aurora contributes a larger share during active times (compared to other auroral types), particularly for the auroral bulge.
5) During the substorm expansion phase, about 50% of the Alfvén wave power over the entire nightside auroral zone is collocated with the auroral bulge region.
6) The widespread expansion of the storm aurora is also observed for the storm Alfvénic oval.

It is worth repeating that these key results are statements about the average behavior of the Alfvénic oval, and that the focus in the dynamic description has been on energy flux. Not only is energy a key component in any physical system, but it allows for the comparison between Alfvén waves and Alfvénic electrons. The Alfvénic energy budget is one component within the total energy budget. We can thus ask: "What role does the global Alfvénic oval deposition rate, here called U_{AW}, play in the overall energy budget rate of the magnetosphere?" Akasofu (1981) listed three major components (not including energy loss *via* plasmoids in the magnetotail), described by the equation: $U_T = U_R + U_J + U_A$. U_R is the energy injection rate into the ring current, U_J is the Joule heating rate in the ionosphere, and U_A is the kinetic energy rate of precipitating auroral particles. U_{AW} is not a new energy rate to be added to the total energy consumption rate; rather, it is already contained within U_A and U_J. Alfvén waves provide an intermediate step in the solar wind-magnetosphere-ionosphere coupling that has not been fully appreciated in the energy description. For example, the estimates provided in this review could be added to the list of energy budgets provided by Baker et al. (1997), where auroral precipitation is listed with 1–10 GW, and ionospheric Joule heating is listed with 10–100 GW. While the Alfvénic contribution, as reviewed here, to the former is significant, it is small for the latter.

There is one complication with incorporating the Alfvénic energy budget into the overall energy budget, which should be stressed. The Alfvénic oval does not only undergo changes along the magnetic field lines inside the AAR (such changes motivated us to define the primary, secondary, and tertiary Alfvénic ovals), but evidence also exists that significant wave dissipation already occurs before the magnetospheric waves reach the AAR. This implies that the total Alfvénic oval power in the magnetosphere is larger than that at the topside of the AAR, which has been the preferred location for observations. In fact, the Alfvénic oval extends to the equatorial region and various boundary regions, including the reconnection region, all of which are generator regions of Alfvén waves. Assessing such a remote Alfvénic oval in its entirety is far from easy, and very likely impossible. However, it does raise the intriguing question of how much power is transported *via* Alfvén waves in the entire magnetosphere, and how this power flow compares to other energy carriers. This is a topic for the future.

Another aspect has not been appreciated for a global energy analysis, but ignoring it might make any energy budget calculations less accurate. It is known from observations and simulations that Alfvénic electron acceleration on auroral field lines generates bidirectional (up- and down-going) electron beams, with most of the acceleration taking place in the direction of wave propagation (Chaston et al., 2003; Watt and Rankin, 2012). While in the study by Chaston et al. (2003) it was shown that the down-going electrons far outnumber the up-going events at FAST altitudes (i.e., below the AAR), it is unknown what the relative relevance above the AAR is. In general, we lack information on the global energy flux by down-going Alfvénic electrons entering the AAR at the topside, that is, electrons that have been accelerated above the AAR, or possibly in the AAR of the other hemisphere as upward-accelerated electrons. The extent to which these components add to the overall Alfvénic energy budget in M-I coupling is unknown. This type of analysis is thus beyond the scope of this review.

It is important to recall that the studies reviewed herein allowed us to entirely ignore the interior of the AAR; the AAR is treated as a black box. Nonetheless, the consistency of the results between observations above and below the AAR support the energy transfer scenario of Alfvénic coupling inside the AAR, as illustrated in Fig. 7. Ultimately, there is a need to study the interior of the AAR with regard to distributions and dissipation along field lines, which also applies to the Alfvénic oval. New multi-satellite auroral missions are required to fill many knowledge gaps with regard to the inner operations of the AAR. One goal of this review has been to provide an energy balance viewpoint for these future missions, by providing boundary conditions on energy fluxes.

Finally, the study of the Alfvénic oval demands further consideration, especially for dynamic (short timescale) changes in the magnetosphere that are prone to the generation of Alfvén waves. After all, the Alfvénic oval is more dynamic than the "quasistatic oval". There are (at least) five areas in which we need to advance our understanding of the Alfvénic oval: (1) Instantaneous observations of the tertiary Alfvénic oval with space imagers would be highly desirable in order to be able to infer Alfvénic processes in the magnetosphere from the aurora. This is also important to quantitatively assess the global Alfvénic impact on the aurora. (2) We have reviewed the phenomenology as it relates to the bottom and topside boundaries of the AAR, which are convenient places as wave energy is funneled through them. However, it would be useful to ascertain the detailed processes involved inside the AAR that lead to the changes of the different layers of the Alfvénic oval. (3) It would be desirable to uncover how the Alfvénic oval extends into the distant magnetosphere, where the generation of the waves occurs, also with the objective of obtaining some estimate of the total magnetospheric Alfvén wave power. (4) Statistical studies above the AAR have focused on the MHD regime. While evidence suggests that this is the energetically dominant component, evidence also shows that the kinetic regime plays a role in energy transport and thus should be investigated statistically as well. (5) A useful extension of this review would be to contrast the dynamic behavior of the Alfvénic oval with that of others, such as Birkeland currents, quasi-static aurora and diffuse aurora, ion outflow, and more, all of which are related to the auroral oval.

Declaration of competing interest

The authors declare that they have no known competing financial interests or personal relationships that could have appeared to influence the work reported in this paper.

Acknowledgement

This work was supported by the NSF grant AGS-2016788. We thank the reviewers for their constructive and helpful comments.

References

Ahn, B.-H., Akasofu, S.-I., Kamide, Y., 1983. The Joule heat production rate and the particle energy injection rate as a function of the geomagnetic indices AE and AL. J. Geophys. Res. 88, 6275–6287.

Akasofu, S.-I., 1964. The development of auroral substorm, *Planet*. Space. Sci. 12, 273–282.

Akasofu, S.-I., Chapman, S., 1963. Magnetic storms: the simultaneous development of the main phase (DR) and of polar magnetic substorms (DP). J. Geophys. Res. 68 (10), 3155–3158.

Akasofu, S.-I., May 1989. The dynamic aurora. Sci. Am. 90–97.

Akasofu, S.-I., 1981. Energy coupling between the solar wind and the magnetosphere. Space Sci. Rev. 28, 121–190.

Akasofu, S.-I., 2001. Predicting geomagnetic storms as a space weather project. In: Space Weather, Monograph, 125. AGU.

Akasofu, S.-I., 2012. Auroral morphology: a historical account and major auroral features during auroral substorms. In: Keiling, A., Donovan, E., Bagenal, F., Karlsson, T. (Eds.), Auroral Phenomenology and Magnetospheric Processes: Earth and Other Planets, vol. 197. Geophys. Monogr. Ser., AGU, Washington, D. C, pp. 29–38. https://doi.org/10.1029/2011GM001156.

Alm, L., Li, B., Marklund, G.T., Karlsson, T., 2015. Statistical altitude distribution of the auroral density cavity. J. Geophys. Res. Space Phys. 120, 996–1006. https://doi.org/10.1002/2014JA020691.

Baker, D.N., Pulkkinen, T.I., Hesse, M., McPherron, R.L., 1997. A quantitative assessment of energy storage and release in the Earth's magnetotail. J. Geophys. Res. 102, 7159–7168.

Boteler, D.H., 2019. A 21st century view of the March 1989 magnetic storm. Space Weather 17, 1427–1441. https://doi.org/10.1029/2019SW002278.

Burch, J.L., 2001. The fury of space storms. Sci. Am. 284, 86–94.

Chapman, S., 1957. The aurora in middle and low latitudes. Nature 179, 7–11.

Chaston, C.C., Bonnell, J.W., Peticolas, L.M., Carlson, C.W., McFadden, J.P., 2002. Driven Alfvén waves and electron acceleration: a FAST case study. Geophys. Res. Lett. 29 (11), 1535. https://doi.org/10.1029/2001GL013842.

Chaston, C.C., Bonnell, J.W., Carlson, C.W., McFadden, J.P., Ergun, R.E., Strangeway, R. J., 2003. Properties of small-scale Alfvén waves and accelerated electrons from FAST. J. Geophys. Res. 108 (A4), 8003. https://doi.org/10.1029/2002JA009420.

Chaston, C.C., et al., 2005. Energy deposition by Alfvén waves into the dayside auroral oval: Cluster and FAST observations. J. Geophys. Res. 110, A02211. https://doi.org/10.1029/2004JA010483.

Chaston, C.C., 2006. ULF waves and auroral electrons. In: Magnetospheric ULF Waves: Synthesis and New Directions Geophysical Monograph Series. American Geophysical Union. https://doi.org/10.1029/169GM16.

Chaston, C.C., Carlson, C.W., McFadden, J.P., Ergun, R.E., Strangeway, R.J., 2007. How important are dispersive Alfvén waves for auroral particle acceleration? Geophys. Res. Lett. 34, L07101. https://doi.org/10.1029/2006GL029144.

Chaston, C., et al., 2008. Turbulent heating and cross-field transport near the magnetopause from THEMIS. Geophys. Res. Lett. 35, L17S08. https://doi.org/10.1029/2008GL033601.

Chaston, C.C., Seki, K., Sakanoi, T., Asamura, K., Hirahara, M., 2010. Motion of aurorae. Geophys. Res. Lett. 37, L08104. https://doi.org/10.1029/2009GL042117.

Chaston, C.C., Bonnell, J.W., Kletzing, C.A., Hospodarsky, G.B., Wygant, J.R., Smith, C. W., 2015. Broadband low-frequency electromagnetic waves in the inner magnetosphere. J. Geophys. Res. Space Phys. 120, 8603–8615. https://doi.org/10.1002/2015JA021690.

Davis, T., Sugiura, M., 1966. Auroral electrojet activity index AE and its universal time variations. J. Geophys. Res. 71, 785–801.

Dombeck, J., Cattell, C., Wygant, J.R., Keiling, A., Scudder, J., 2005. Alfvén waves and Poynting flux observed simultaneously by Polar and FAST in the plasma sheet boundary layer. J. Geophys. Res. 110, A12S90. https://doi.org/10.1029/2005JA011269.

Dombeck, J., Cattell, C., Prasad, N., Meeker, E., Hanson, E., McFadden, J., 2018. Identification of auroral electron precipitation mechanism combinations and their relationships to net downgoing energy and number flux. J. Geophys. Res.: Space Phys. 123 https://doi.org/10.1029/2018JA025749.

Fedorov, E.N., et al., 2004. Alfvén wave modulation of the auroral acceleration region. Earth Planets Space 56, 649–661, 2004.

Feldstein, Y.I., 1963. The morphology of aurorae and geomagnetism. In: Bagarjatsky, B. A., Krasovsky, V.I. (Eds.), Aurorae and Airglow, No. 10. Academy of Sciences of the USSR, Moscow, pp. 121–125.

Feldstein, Y.I., Galperin, Y.I., 1985. The auroral luminosity structure in the high-latitude upper atmosphere: its dynamics and relationship to the large-scale structure of the Earth's magnetosphere. Rev. Geophys. 23 (3), 217–275.

Feldstein, Y.I., Starkov, G.V., 1967. Dynamics of auroral belt and polar geomagnetic disturbances. Planet. Space Sci. 15, 209–229. https://doi.org/10.1016/0032-0633(67)90190-0.

Forsyth, C., et al., 2014. In situ spatiotemporal measurements of the detailed azimuthal substructure of the substorm current wedge. J. Geophys. Res. Space Phys. 119, 927–946. https://doi.org/10.1002/2013JA019302.

Forsyth, C., Fazakerley, A.N., 2012. Multispacecraft observations of auroral acceleration by Cluster. In: Keiling, A., et al. (Eds.), *Auroral Phenomenology and Magnetospheric Processes: Earth and Other Planets*, Geophys. Monogr. Ser., vol. 197. AGU, Washington, D. C, pp. 261–270. https://doi.org/10.1029/2011GM001166.

Glassmeier, K.-H., Carsten, C., Cramm, R., et al., 1999. Magnetospheric field line resonances: a comparative planetology approach. Surv. Geophys. 20, 61–109.

Gonzalez, W.D., Joselyn, J.A., Kamide, Y., Kroehl, H.W., Rostoker, G., Tsurutani, B.T., Vasyliunas, V.M., 1994. What is a geomagnetic storm? J. Geophys. Res. 99, 5771–5792.

Hatch, S.M., LaBelle, J., Lotko, W., Chaston, C.C., Zhang, B., 2017. IMF control of Alfvénic energy transport and deposition at high latitudes. J. Geophys. Res.: Space Phys. 122, 12,189–12,211.

Hatch, S.M., LaBelle, J., Lotko, W., Chaston, C.C., 2018. Storm phase-partitioned rates and budgets of global Alfvénic energy deposition, electron precipitation, and ion outflow. J. Atmos. Sol. Terr. Phys. 167, 1–12.

Hull, A.J., Chaston, C.C., Frey, H.U., Fillingim, M.O., Goldstein, M.L., Bonnell, J.W., Mozer, F.S., 2016. The "Alfvénic surge" at substorm onset/expansion and the formation of "Inverted Vs": Cluster and IMAGE observations. J. Geophys. Res. Space Phys. 121, 3978–4004. https://doi.org/10.1002/2015JA022000.

Ivchenko, N.E., Marklund, G., 2001. Observation of low frequency electromagnetic activity at 1000 km altitude. Ann. Geophys. 19, 643–648.

Ivchenko, N., Blixt, E.M., Lanchester, B.S., 2005. Multispectral observations of auroral rays and curls. Geophys. Res. Lett. 32, L18106. https://doi.org/10.1029/2005GL022650.

Janhunen, P., et al., 2006. Alfvénic electron acceleration in aurora occurs in global Alfvén resonosphere region. Space Sci. Rev. 122, 89–95.

Johnson, J.R., Cheng, C.Z., Song, P., 2001. Signatures of mode conversion and kinetic Alfvén waves at the magnetopause. Geophys. Res. Lett. 28, 227.

Kan, J.R., Lee, L.C., 1979. Energy coupling function and solar wind-magnetosphere dynamo. Geophys. Res. Lett. 6, 577–580. https://doi.org/10.1029/GL006i007p00577.

Karlsson, T., 2012. The acceleration region of stable Auroral arcs. In: Keiling, A., Donovan, E., Bagenal, F., Karlsson, T. (Eds.), Auroral Phenomenology and Magnetospheric Processes: Earth and Other Planets, vol. 197, pp. 227–239. https://doi.org/10.1029/2011GM001179.

Karlsson, T., Kullen, A., Marklund, G., 2017. Dawn-dusk asymmetries in auroral morphology and processes. In: Haaland, S., Runov, A., Forsyth, C. (Eds.), Dawn-Dusk Asymmetries in Planetary Plasma Environments. https://doi.org/10.1002/9781119216346.ch23.

Keiling, A., Wygant, J.R., Cattell, C.A., Temerin, M., Mozer, F.S., Kletzing, C.A., Scudder, J.D., Russell, C.T., Lotko, W., Streltsov, A.V., 2000. Large Alfvén wave power in the plasma sheet boundary layer during the expansion phase of substorms. Geophys. Res. Lett. 27, 3169–3173.

Keiling, A., Wygant, J.R., Cattell, C., Peria, W., Parks, G., Temerin, M., Mozer, F.S., Russell, C.T., Kletzing, C.A., 2002. Correlation of Alfvén wave Poynting flux in the plasma sheet at 4-7 RE with ionospheric electron energy flux. J. Geophys. Res. 107 (A7), 1132. https://doi.org/10.1029/2001JA900140.

Keiling, A., Wygant, J.R., Cattell, C.A., Mozer, F.S., Russell, C.T., 2003. The global morphology of wave Poynting flux: powering the aurora. Science 299, 383. https://doi.org/10.1126/science.1080073.

Keiling, A., Parks, G.K., Wygant, J.R., Dombeck, J., Mozer, F.S., Russell, C.T., Streltsov, A.V., Lotko, W., 2005. Some properties of Alfvén waves: observations in the tail lobes and the plasma sheet boundary layer. J. Geophys. Res. 110, A10S11. https://doi.org/10.1029/2004JA010907.

Keiling, A., 2009. Alfvén waves and their roles in the dynamics of the Earth's magnetotail: a review. Space Sci. Rev. 142, 73–156. https://doi.org/10.1007/s11214-008-9463-8.

Keiling, A., et al., 2012. Auroral Phenomenology and Magnetospheric Processes: Earth and Other Planets, vol. 197. American Geophysical Union. https://doi.org/10.1029/GM197.

Keiling, A., Thaller, S., Wygant, J., Dombeck, J., 2019a. Assessing the global Alfvén wave power flow into and out of the auroral acceleration region during geomagnetic storms. Sci. Adv. 5, eaav8411 https://doi.org/10.1126/sciadv.aav8411.

Keiling, A., Thaller, S., Wygant, J., Dombeck, J., 2019b. Global Alfvén wave power in the auroral zone in relation to the AE index. J. Geophys. Res. Space Phys. 124 https://doi.org/10.1029/2019JA026805.

Keiling, A., Thaller, S., Dombeck, J., Wygant, J., 2020. Temporal evolution of substorm-driven global Alfvén wave power above the auroral acceleration region. J. Geophys. Res.: Space Phys. 125, e2019JA027444.

Kletzing, C.A., Hu, S., 2001. Alfvén wave generated electron time dispersion. Geophys. Res. Lett. 28, 693–696.

Lee, A.R., Newell, P.T., Gjerloev, J., Liou, K., 2010. Relatively low-latitude wave aurora and substorms. Geophys. Res. Lett. 37, L06101. https://doi.org/10.1029/2009GL041680.

Liang, J., Donovan, E., Jackel, B., Spanswick, E., Gillies, M., 2016. On the 630 nm red-line pulsating aurora: red-line Emission Geospace Observatory observations and model simulations. J. Geophys. Res. Space Phys. 121, 7988–8012. https://doi.org/10.1002/2016JA022901.

Liou, K., Newell, P.T., Meng, C.-I., Brittnacher, M., Parks, G., 1997. Synoptic auroral distribution: a survey using Polar ultraviolet imagery. J. Geophys. Res. 102 (A12), 27197–27205.

Liou, K., Newell, P.T., Zhang, Y.-L., Paxton, L.J., 2013. Statistical comparison of isolated and non-isolated auroral substorms. J. Geophys. Res. Space Phys. 118, 2466–2477.

Liou, K., Takahashi, K., 2013. Observations of field line resonance with global auroral images. J. Atmos. Sol. Terr. Phys. 105–106, 152–159.

Lotko, W., 2004. Inductive magnetosphere-ionosphere coupling. J. Atmos. Sol. Terr. Phys. 66, 1443–1456.

Lynch, K.A., Hampton, D., Mella, M., Zhang, B., Dahlgren, H., Disbrow, M., Kintner, P.M., Lessard, M., Lundberg, E., Stenbaek-Nielsen, H.C., 2012. Structure and dynamics of the nightside poleward boundary: sounding rocket and ground-based observations of auroral electron precipitation in a rayed curtain. J. Geophys. Res. 117, A11202. https://doi.org/10.1029/2012JA017691.

Lyon, J.G., Fedder, J.A., Mobarry, C.M., 2004. The Lyon-Fedder-Mobarry (LFM) global MHD magnetospheric simulation code. J. Atmos. Sol. Terr. Phys. 66 (15–16), 1333–1350. https://doi.org/10.1016/j.jastp.2004.03.020.

Lysak, R.L., Song, Y., 2005. Nonlocal interactions between electrons and Alfvén waves on auroral field lines. J. Geophys. Res. 110, A10S06. https://doi.org/10.1029/2004JA010803.

Marklund, G., Ivchenko, N., Karlsson, T., et al., 2001. Temporal evolution of the electric field accelerating electrons away from the auroral ionosphere. Nature 414, 724–727. https://doi.org/10.1038/414724a.

Mauk, B., Bagenal, F., 2012. Comparative auroral physics: Earth and other planets. In: Keiling, A., Donovan, E., Bagenal, F., Karlsson, T. (Eds.), Auroral Phenomenology and Magnetospheric Processes: Earth and Other Planets, vol. 197.

Maynard, N.C., Burke, W.J., Basinska, E.M., Erickson, G.M., Hughes, W.J., Singer, H.J., Yahnin, A.G., Hardy, D.A., Mozer, F.S., 1996. Dynamics of the inner magnetosphere near times of substorm onset. J. Geophys. Res. 101, 7705–7736.

Mende, S.B., Carlson, C.W., Frey, H.U., Peticolas, L.M., Østgaard, N., 2003. FAST and IMAGE-FUV observations of a substorm onset. J. Geophys. Res. 108 (A9), 1344. https://doi.org/10.1029/2002JA009787.

Mende, S.B., Harris, S.E., Frey, H.U., Angelopoulos, V., Russell, C.T., Donovan, E., et al., 2008. The THEMIS array of ground-based observatories for the study of auroral substorms. Space Sci. Rev. 141 (1-4), 357–387. https://doi.org/10.1007/s11214-008-9380-x.

Mende, S.B., 2016. Observing the magnetosphere through global auroral imaging: 1. Observables, J. Geophys. Res. Space Phys. 121, 10,623–10,637. https://doi.org/10.1002/2016JA022558.

Mella, M.R., Lynch, K.A., Hampton, D.L., Dahlgren, H., Kintner, P.M., Lessard, M., Lummerzheim, D., Lundberg, E.T., Nicolls, M.J., Stenbaek-Nielsen, H.C., 2011. Sounding rocket study of two sequential auroral poleward boundary intensifications. J. Geophys. Res. 116, A00K18. https://doi.org/10.1029/2011JA016428.

Meng, C.-I., Liou, K., 2002. Global auroral power as an index for geospace disturbances. Geophys. Res. Lett. 29 (12) https://doi.org/10.1029/2001GL013902, 41-1.

Merkin, V.G., Lyon, J.G., 2010. Effects of the low-latitude ionospheric boundary condition on the global magnetosphere. J. Geophys. Res. 115, A10202.

Milan, S.E., et al., 2009. Influence on the radius of the auroral oval. Ann. Geophys. 27, 2913–2924, 2009.

Mitchell, E.J., Newell, P.T., Gjerloev, J.W., Liou, K., 2013. OVATION-SM: a model of auroral precipitation based on SuperMAG generalized auroral electrojet and substorm onset times. J. Geophys. Res. Space Phys. 118, 3747–3759. https://doi.org/10.1002/jgra.50343.

Mottez, F., 2016. Relationship between Alfvén wave and quasi-static acceleration in earth's auroral zone. In: Keiling, A., Lee, D.-H., Nakariakov, V. (Eds.), Low-Frequency Waves in Space Plasmas. https://doi.org/10.1002/9781119055006.ch8.

Mozer, F.S., Hull, A., 2001. Origin and geometry of upward parallel electric fields in the auroral acceleration region. J. Geophys. Res. 106, 5763–5778.

Newell, P.T., et al., 2001. Auroral precipitation power during substorms: a Polar UV Imager-based superposed epoch analysis. J. Geophys. Res. 106, 28,885–28,896.

Newell, P.T., Sotirelis, T., Liou, K., Meng, C.-I., Rich, F.J., 2007. A nearly universal solar wind-magnetosphere coupling function inferred from 10 magnetospheric state variables. J. Geophys. Res. 112, A01206. https://doi.org/10.1029/2006JA012015.

Newell, P.T., Sotirelis, T., Wing, S., 2009. Diffuse, monoenergetic, and broadband aurora: the global precipitation budget. J. Geophys. Res. 114, A09207. https://doi.org/10.1029/2009JA014326.

Newell, P.T., Lee, A.R., Liou, K., Ohtani, S.-I., Sotirelis, T., Wing, S., 2010. Substorm cycle dependence of various types of aurora. J. Geophys. Res. 115, A09226. https://doi.org/10.1029/2010JA015331.

Newell, P.T., Gjerloev, J.W., 2011. Evaluation of SuperMAG auroral electrojet indices as indicators of substorms and auroral power. J. Geophys. Res. 116, A12211. https://doi.org/10.1029/2011JA016779.

Newell, P.T., Gjerloev, J.W., 2014. Local geomagnetic indices and the prediction of auroral power. J. Geophys. Res. Space Phys. 119, 9790–9803. https://doi.org/10.1002/2014JA020524.

Nishimura, Y., Kikuchi, T., Shinbori, A., Wygant, J., Tsuji, Y., Hori, T., Ono, T., Fujita, S., Tanaka, T., 2010. Direct measurements of the Poynting flux associated with convection electric fields in the magnetosphere. J. Geophys. Res. 115, A12212.

Osaki, H., Takahashi, K., Fukunishi, H., Nagatsuma, T., Oya, H., Matsuoka, A., Milling, D. K., 1998. Pi2 pulsations observed from the Akebono satellite in the plasmasphere. J. Geophys. Res. 103 (17), 605.

Østgaard, N., Vondrak, R.R., Gjerloev, J.W., Germany, G., 2002. A relation between the energy deposition by electron precipitation and geomagnetic indices during substorms. J. Geophys. Res. 107 (A9), 1246. https://doi.org/10.1029/2001JA002003.

Perry, S.J., 1880. Aurora borealis and magnetic storms. Nature 22, 361.

Palmroth, M., Grandin, M., Helin, M., Koski, P., Oksanen, A., Glad, M.A., et al., 2020. Citizen scientists discover a new auroral form: dunes provide insight into the upper atmosphere. AGU Advances 1, e2019AV000133. https://doi.org/10.1029/2019AV000133.

Pilipenko, V., Fedorov, E., Engebretson, M.J., Yumoto, K., 2004. Energy budget of Alfvén wave interactions with the auroral acceleration region. J. Geophys. Res. 109, A10204. https://doi.org/10.1029/2004JA010440.

Saito, T., 1969. Geomagnetic pulsations. Space Sci. Rev. 10, 319–412.

Shue, J.-H., Newell, P.T., Liou, K., Meng, C.-I., 2001. Influence of interplanetary magnetic field on global auroral patterns. J. Geophys. Res. 106 (A4), 5913–5926.

Song, Y., Lysak, R.L., 2006. Displacement current and the generation of parallel electric fields. Phys. Rev. Lett. https://doi.org/10.1103/PhysRevLett.96.145002.

Southwood, D.J., Hughes, W.J., 1983. Theory of hydromagnetic waves in the magnetosphere. Space Sci. Rev. 35, 301–366. https://doi.org/10.1007/BF00169231.

Stasiewicz, K., et al., 2000. Small-scale Alfvénic structure in the aurora. Space Sci. Rev. 92, 423–533.

Takada, T., et al., 2006. Alfvén waves in the near-PSBL lobe: Cluster observations. Ann. Geophys. 24, 1001–1013.

Takahashi, K., et al., 1988. AMPTE/CCE observations of substorm-associated standing Alfvén waves in the midnight sector. Geophys. Res. Lett. 15, 1287.

Torr, M.R., et al., 1995. A far ultraviolet imager for the international solar-terrestrial physics mission. In: The Global Geospace Mission. Springer, New York, pp. 459–495.

Vaivads, A., et al., 2003. What high altitude observations tell us about the auroral acceleration: a Cluster/DMSP conjunction. Geophys. Res. Lett. 30 (3), 1106. https://doi.org/10.1029/2002GL016006.

Watt, C.E.J., Rankin, R., 2012. Alfven wave acceleration of auroral electrons in warm magnetospheric plasma. In: Keiling, A., Donovan, E., Bagenal, F., Karlsson, T. (Eds.), Auroral Phenomenology and Magnetospheric Processes: Earth and Other Planets 197, 251–260.

Watt, C.E.J., Rankin, R., Rae, I.J., Wright, D.M., 2005. Self-consistent electron acceleration due to inertial Alfvén wave pulses. J. Geophys. Res. 110, A10S07. https://doi.org/10.1029/2004JA010877.

Wing, S., Gkioulidou, M., Johnson, J.R., Newell, P.T., Wang, C.-P., 2013. Auroral particle precipitation characterized by the substorm cycle. J. Geophys. Res. Space Phys. 118, 1022–1039. https://doi.org/10.1002/jgra.50160.

Wygant, J.R., Keiling, A., Cattell, C.A., Johnson, M., Lysak, R.L., Temerin, M., Mozer, F., Kletzing, C.A., Scudder, J.D., Peterson, W., Russell, C.T., Parks, G., Germany, G., 2000. Polar spacecraft-based comparisons of intense electric fields and Poynting flux near and within the plasma sheet-tail lobe boundary to UVI images: an energy source for the aurora. J. Geophys. Res. 105, 18,675–18,692.

Wygant, J.R., Keiling, A., et al., 2002. Evidence for kinetic Alfvén waves and parallel electron energization at 4–6 RE altitudes in the plasma sheet boundary layer. J. Geophys. Res. 107 (A8), 1201. https://doi.org/10.1029/2001JA900113.

Yao, Y., Chaston, C.C., Glassmeier, K.-H., Angelopoulos, V., 2011. Electromagnetic waves on ion gyro-radii scales across the magnetopause. Geophys. Res. Lett. 38, L09102. https://doi.org/10.1029/2011GL047328.

Zhang, Y., Paxton, L.J., 2008. An empirical Kp-dependent global auroral model based on TIMED/GUVI FUV data. J. Atmos. Sol. Terr. Phys. 70, 1231. https://doi.org/10.1016/j.jastp.2008.03.008.

Zhang, Y., Paxton, L.J., 2016. Auroral Dynamics and Space Weather, vol. 215. American Geophysical Union. https://doi.org/10.1002/9781118978719.

Zhang, B., Lotko, W., Brambles, O., Damiano, P., Wiltberger, M., Lyon, J., 2012. Magnetotail origins of auroral Alfvénic power. J. Geophys. Res. 117, A09205. https://doi.org/10.1029/2012JA017680.

Zhang, B., Lotko, W., Brambles, O., Xi, S., Wiltberger, M., Lyon, J., 2014. Solar wind control of auroral Alfvénic power generated in the magnetotail. J. Geophys. Res. Space Phys. 119 https://doi.org/10.1002/2013JA019178.

Zhang, B., Lotko, W., Brambles, O., Wiltberger, M., Lyon, J., 2015. Electron precipitation models in global magnetosphere simulations. J. Geophys. Res. Space Phys. 120, 1035–1056. https://doi.org/10.1002/2014JA020615.

Zheng, Y., Rastaetter, L., 2016. Space Weather Products and Tools Used in Auroral Monitoring and Forecasting at CCMC/SWRC.